

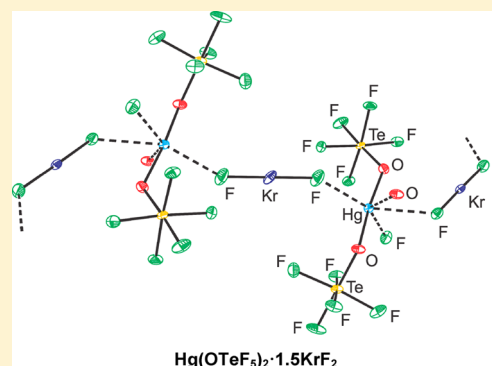
Noble-Gas Difluoride Complexes of Mercury(II): The Syntheses and Structures of $\text{Hg}(\text{OTeF}_5)_2 \cdot 1.5\text{NgF}_2$ ($\text{Ng} = \text{Xe}, \text{Kr}$) and $\text{Hg}(\text{OTeF}_5)_2$

John R. DeBackere, H  l  ne P. A. Mercier, and Gary J. Schrobilgen*

Department of Chemistry, McMaster University, Hamilton, Ontario, L8S 4M1, Canada

S Supporting Information

ABSTRACT: The synthesis of high-purity $\text{Hg}(\text{OTeF}_5)_2$ has resulted in its structural characterization in the solid state by Raman spectroscopy and single-crystal X-ray diffraction (XRD) and in solution by ^{19}F NMR spectroscopy. The crystal structure of $\text{Hg}(\text{OTeF}_5)_2$ (-173°C) consists of discrete $\text{Hg}(\text{OTeF}_5)_2$ units having *gauche*-conformations that interact through long $\text{Hg}\cdots\text{O}$ and $\text{Hg}\cdots\text{F}$ intramolecular contacts to give a chain structure. The Lewis acidity of $\text{Hg}(\text{OTeF}_5)_2$ toward NgF_2 ($\text{Ng} = \text{Xe}, \text{Kr}$) was investigated in SO_2ClF solvent and shown to form stable coordination complexes with NgF_2 at -78°C . Both complexes were characterized by low-temperature Raman spectroscopy (-155°C) and single-crystal XRD. The complexes are isostructural and are formulated as $\text{Hg}(\text{OTeF}_5)_2 \cdot 1.5\text{NgF}_2$. The $\text{Hg}(\text{OTeF}_5)_2$ units of $\text{Hg}(\text{OTeF}_5)_2 \cdot 1.5\text{NgF}_2$ also have *gauche*-conformations and are linked through bridging NgF_2 molecules, also resulting in chain structures. These complexes represent the only examples of coordination compounds where NgF_2 coordinates to mercury in a neutral covalent compound and the only example of mercury coordinated to KrF_2 . Moreover, the $\text{Hg}(\text{OTeF}_5)_2 \cdot 1.5\text{KrF}_2$ complex is the only KrF_2 complex known to contain a bridging KrF_2 ligand. Energy-minimized gas-phase geometries and vibrational frequencies for the model compounds, $[\text{Hg}(\text{OTeF}_5)_2]_3$ and $[\text{Hg}(\text{OTeF}_5)_2]_3 \cdot 2\text{NgF}_2$, were obtained and provide good approximations of the local environments of $\text{Hg}(\text{OTeF}_5)_2$ and NgF_2 in the crystal structures of $\text{Hg}(\text{OTeF}_5)_2$ and $\text{Hg}(\text{OTeF}_5)_2 \cdot 1.5\text{NgF}_2$. Assignments of the Raman spectra of $\text{Hg}(\text{OTeF}_5)_2$ and $\text{Hg}(\text{OTeF}_5)_2 \cdot 1.5\text{NgF}_2$ are based on the calculated vibrational frequencies of the model compounds. Natural bond orbital analyses provided the associated bond orders, valencies, and natural population analysis charges.



INTRODUCTION

The fluoride-ion donor behavior of noble-gas difluorides toward strong fluoride ion acceptors such as AsF_5 and SbF_5 is well established, with several examples of NgF^+ and Ng_2F_3^+ ($\text{Ng} = \text{Xe}, \text{Kr}$) salts having been characterized in the solid state and in solution.^{1–3} Avoidance of “complete” fluoride transfer requires the corresponding Lewis acid center to be weak to moderate in strength and oxidatively resistant. In the case of XeF_2 , two coordination modalities, terminal and bridging, have been observed.¹ Both fluorine atoms of XeF_2 may coordinate to two Lewis acid centers to give a bridging XeF_2 ligand, or a single fluorine atom of XeF_2 may coordinate to give a terminal XeF_2 ligand. Examples of both coordination modalities are known with XeF_2 coordinated to a nonmetal ($[\text{BrOF}_2][\text{AsF}_6] \cdot 2\text{XeF}_2$)⁴ and to metal cation centers (Li^+ , Mg^{2+} , Ca^{2+} , Cu^{2+} , Zn^{2+} , Sr^{2+} , Ag^+ , Cd^{2+} , Ba^{2+} , La^{3+} , Nd^{3+} , and Pb^{2+}).^{5–9} The majority of these complexes have been structurally characterized by single-crystal X-ray diffraction. Among the group 12 metal cation complexes of XeF_2 that have been structurally characterized are $\text{Cd}(\text{XeF}_2)(\text{BF}_4)_2$,⁷ $\text{Cd}_2(\text{XeF}_2)_{10}(\text{SbF}_6)_4$,⁹ $\text{Cd}(\text{XeF}_2)_4(\text{AsF}_6)_2$,¹⁰ $\text{Cd}(\text{XeF}_2)_5(\text{PF}_6)_2$,¹¹ and $\text{Zn}(\text{XeF}_2)_6(\text{SbF}_6)_2$.¹² Preliminary X-ray crystal structures and Raman studies of the Hg^{2+} cation complexes $\text{Hg}(\text{XeF}_2)_5(\text{AsF}_6)_2$ ¹³ and $\text{Hg}(\text{XeF}_2)_5(\text{SbF}_6)_2$ ¹⁴ have also been

reported. In contrast, examples of KrF_2 coordination complexes are very rare. The complex, $[\text{BrOF}_2][\text{AsF}_6] \cdot 2\text{KrF}_2$, represents the first KrF_2 coordination complex to have been structurally characterized by X-ray crystallography and contains two terminally coordinated KrF_2 molecules.¹⁵ Several terminally coordinated NgF_2 complexes of group 6 d^0 transition-metal oxide tetrafluorides, i.e., $\text{XeF}_2 \cdot n\text{MOF}_4$ ($n = 1–3$, $\text{M} = \text{W}$,^{16,17} Mo ;¹⁷ $n = 4$, $\text{M} = \text{Mo}$ ¹⁷) and $\text{KrF}_2 \cdot n\text{MOF}_4$ ($n = 1$, $\text{M} = \text{W}$,¹⁸ Mo ,¹⁸ Cr ¹⁹); $n = 2–3$, $\text{M} = \text{Mo}$ ¹⁸) have also been synthesized and characterized in the solid state by Raman spectroscopy and/or in solution by ^{19}F and ^{129}Xe multi-NMR spectroscopy. A low-precision, room-temperature X-ray crystal structure of $\text{XeF}_2 \cdot \text{WOF}_4$ has also been reported.²⁰

The pentafluoro-orthotellurate group, $-\text{OTeF}_5$, may be regarded as a bulky fluorine analogue having a group electronegativity (3.88²¹ and 3.87²²) comparable to that of fluorine (3.98, Allred-Rochow scale). Negative charge dispersal over its five fluorine and an oxygen atom results in a ligand group of low nucleophilicity and high oxidative resistance.²³ The steric bulk and propensity of the $-\text{OTeF}_5$ group not to extensively oxygen bridge but to bond in a monodentate

Received: November 29, 2013

Published: February 3, 2014

fashion,^{24–26} is expected to result in molecular species that have smaller mercury coordination numbers in the solid state than its fluorine analogue, HgF₂, which possesses a three-dimensional, networked structure (CN = 8, fluorite structure).²⁷ Overall, the less crowded coordination environment of Hg(II) in Hg(OTeF₅)₂ provides more space for donor ligand molecules such as NgF₂ to coordinate to Hg(II).

In the present study, Hg(OTeF₅)₂ has been synthesized in high purity and yield, along with its isomorphous noble-gas difluoride coordination complexes, Hg(OTeF₅)₂·1.5NgF₂ (Ng = Xe, Kr), and structurally characterized by low-temperature single-crystal X-ray diffraction, Raman spectroscopy, and quantum-chemical calculations. Mercury(II) bis(pentafluoroorthotellurate(VI)) was also characterized in solution by ¹⁹F NMR spectroscopy in the present and past^{28,29} studies. The present work provides a significant extension of the little studied coordination chemistry of KrF₂ by providing the only example of a bridging KrF₂ molecule that is currently known and insight into the coordination behavior and Lewis acidity of Hg(II) in the neutral Hg(OTeF₅)₂ molecule.

RESULTS AND DISCUSSION

The purities of all products and progress of all reactions were routinely monitored by periodically quenching the reactions at –196 °C and recording the low-temperature Raman spectra (–150 °C) of the reaction mixtures in the solid state or in frozen solutions.

Synthesis of Hg(OTeF₅)₂. The synthesis of Hg(OTeF₅)₂ is based on a modification of prior synthetic procedures^{28,29} and was accomplished by the reaction of high-purity HgF₂ (see Supporting Information) with a small molar excess of HOTeF₅ (1:2.05) at 50 °C for several hours (eq 1). The Raman spectrum of pure Hg(OTeF₅)₂ is provided in Figure S1.



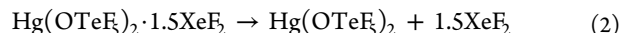
The literature procedures for the synthesis of Hg(OTeF₅)₂ call for purification of the product by sublimation at 180²⁸ or 200 °C.²⁹ In the present work, the Raman spectrum of sublimed Hg(OTeF₅)₂ (135–165 °C) showed several additional weak bands (Figure S2) that do not appear in the Raman spectrum of unsublimed Hg(OTeF₅)₂ (Figure S1), indicating that some decomposition had occurred during sublimation; however, the decomposition products have not been identified. The Raman bands associated with the decomposition products may have been too broad and weak at room temperature to be observed in the prior studies. The main bands observed in the presently reported low-temperature Raman spectrum of the product are in agreement with those previously obtained for Hg(OTeF₅)₂ by room-temperature Raman spectroscopy (CH₂Cl₂ solution)²⁸ and room-temperature infrared spectroscopy (solid in a CsBr pellet²⁸ or in a nujol mull²⁹).

The current synthetic procedure produces Hg(OTeF₅)₂ in high yield and purity without the need for further purification and has allowed its full characterization in the solid state by low-temperature single-crystal X-ray diffraction, Raman spectroscopy, and in solution by ¹⁹F NMR spectroscopy.

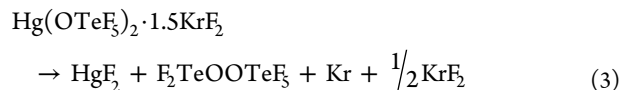
The ¹⁹F (470.568 MHz) NMR spectrum of Hg(OTeF₅)₂ was obtained in CD₂Cl₂ at 25 °C. The spectrum was second order and consisted of an AB₄ pattern with the A resonance (δ_A = –38.4 ppm; ²J(¹⁹F_A–¹⁹F_B) = 185 Hz; ¹J(¹²⁵Te–¹⁹F_A) = 3363 Hz; ¹J(¹²³Te–¹⁹F_A) = 2794 Hz) occurring at high frequency of the B₄ resonance (δ_B = –42.1 ppm; ¹J(¹²⁵Te–¹⁹F_B) = 3603 Hz;

¹J(¹²³Te–¹⁹F_B) = 2982 Hz). The δ_A and δ_B chemical shifts and ²J(¹⁹F_A–¹⁹F_B) coupling constant are in good agreement with the previously reported values: –38.2²⁸ [–38.1],²⁹ –40.1²⁸ [–40.2]²⁹ ppm and 186²⁸ [185]²⁹ Hz in CH₂Cl₂ and –27.8²⁸ [–27.4],²⁹ –40.4²⁸ [–40.3]²⁹ ppm and 180²⁸ [180]²⁹ Hz in CH₃CN. Accurate ¹J(^{123,125}Te–¹⁹F_{A,B}) couplings are reported here for the first time; only one coupling was previously reported (3560 Hz in CH₂Cl₂ and 3580 Hz in CH₃CN) which was described as a J(¹²⁵Te–¹⁹F) coupling but was not specifically assigned to F_A or F_B.²⁸

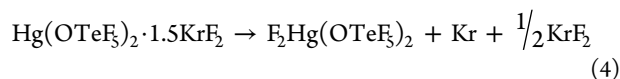
Synthesis of Hg(OTeF₅)₂·1.5XeF₂. The Hg(OTeF₅)₂·1.5XeF₂ complex was synthesized by adding a 1:1.7 molar excess of XeF₂ to Hg(OTeF₅)₂ at –140 °C. Sulfuryl chloride fluoride was condensed onto the mixture at –78 °C, followed by warming to 0 °C for 5 min, whereupon the solid dissolved. The mixture was maintained at –78 °C for 5 days prior to removing the solvent under dynamic vacuum at –78 °C, leaving behind a white solid corresponding to Hg(OTeF₅)₂·1.5XeF₂. When the solid complex was warmed to room temperature under 1 atm of dry N₂, slow dissociation into Hg(OTeF₅)₂ and XeF₂ occurred and was complete within 6 days (eq 2).



Synthesis of Hg(OTeF₅)₂·1.5KrF₂. The Hg(OTeF₅)₂·1.5KrF₂ complex was synthesized by the reaction of Hg(OTeF₅)₂ and KrF₂ (1:2.2 molar ratio) in SO₂ClF solvent. The mixture was warmed to –20 °C for 2 min and then maintained at –78 °C for 3 h. Removal of the solvent at –78 °C resulted in Hg(OTeF₅)₂·1.5KrF₂ as a white solid. When warmed to 0 °C under 1 atm of dry N₂ for 3 h, the Hg(OTeF₅)₂·1.5KrF₂ complex underwent a redox decomposition to form HgF₂, F₅TeOOTeF₅, KrF₂, and Kr according to eq 3. The formation of HgF₂ and F₅TeOOTeF₅ was confirmed by quenching the decomposition reaction in the Raman spectrometer and recording its spectrum at –150 °C. The Raman spectrum showed two strong bands at 254 (HgF₂) and 464 cm^{–1} (KrF₂) as well as bands characteristic of F₅TeOOTeF₅, in particular, a strong band corresponding to the O–O stretch of F₅TeOOTeF₅ appeared at 899 cm^{–1}.



The absence of Hg(OTeF₅)₂ as a decomposition product indicates that oxidative fluorination of Hg(OTeF₅)₂ by KrF₂ rather than dissociation of the complex occurs at elevated temperatures. A previous computational study predicted that HgF₂ and F₅TeOOTeF₅ will be the dominant products resulting from the decomposition of F₂Hg(OTeF₅)₂ (eq 4).³⁰ Thus, the formation of F₂Hg(OTeF₅)₂ as an intermediate in the decomposition pathway of the complex (eqs 4 and 5) cannot be ruled out.



X-ray Crystallography. Details of the data collection parameters and other crystallographic information for Hg(OTeF₅)₂ and Hg(OTeF₅)₂·1.5NgF₂ (Ng = Xe, Kr) are

provided in Table 1 and the bond lengths and angles are listed in Tables 2 and 3.

Table 1. Summary of Crystal Data and Refinement Results for $\text{Hg}(\text{OTeF}_5)_2$ and $\text{Hg}(\text{OTeF}_5)_2 \cdot 1.5\text{NgF}_2$ (Ng = Xe, Kr)

chem formula	$\text{Hg}(\text{OTeF}_5)_2$	$\text{Hg}(\text{OTeF}_5)_2 \cdot 1.5\text{XeF}_2$	$\text{Hg}(\text{OTeF}_5)_2 \cdot 1.5\text{KrF}_2$
space group	$C2/c$	$P2_1/n$	$P2_1/n$
a (Å)	18.681(1)	9.0574(2)	8.7981(4)
b (Å)	8.6489(4)	17.8943(3)	17.4153(9)
c (Å)	5.8008(3)	9.1285(2)	9.2243(4)
β (°)	96.215(3)	114.548(1)	113.788(3)
V (Å ³)	931.74(1)	1345.78(6)	1293.3(2)
Z (molecules/unit cell)	4	2	2
M (g mol ⁻¹)	677.79	931.74	860.49
ρ_{calcd} (g cm ⁻³)	4.832	4.599	4.419
T (°C)	-173	-173	-173
μ (mm ⁻¹)	22.80	19.55	21.57
R_1^a	0.0461	0.0282	0.0284
wR_2^b	0.1232	0.0595	0.0716

^a R_1 is defined as $\sum ||F_o| - |F_c|| / \sum |F_o|$ for $I > 2\sigma(I)$. ^b wR_2 is defined as $[\sum [w(F_o^2 - F_c^2)^2] / \sum w(F_o^2)^2]^{1/2}$ for $I > 2\sigma(I)$.

$\text{Hg}(\text{OTeF}_5)_2$. Unlike the three-dimensional network structure of HgF_2 , the structure of $\text{Hg}(\text{OTeF}_5)_2$ consists of discrete $\text{Hg}(\text{OTeF}_5)_2$ units that interact through long Hg---O and Hg---F intramolecular contacts, resulting in chains that run parallel to the c -axis of its crystallographic unit cell (Figures 1a and S3A). The adjacent chains form isolated layers along the a - and b -axes with no F...F distances between them that are less than the sum of twice the fluorine van der Waals radii (2.94 Å, Figure S3b).

The Hg(II) coordination sphere is a distorted octahedron consisting of secondary Hg---O ($2 \times 2.641(7)$ Å) and slightly longer Hg---F contacts ($2 \times 2.810(7)$ Å) in addition to the primary Hg---O bonds ($2 \times 2.016(6)$ Å), as illustrated in Figure 1b. The Hg---O bonds are *trans* to one another, whereas the Hg---O and Hg---F contacts are *cis* to one another and to the primary Hg---O bonds. The secondary contacts are significantly less than the sums of the van der Waals radii (3.05 Å for Hg...O and 3.06 Å for Hg...F),³¹ indicating significant covalent interactions between Hg(II) and the $-\text{OTeF}_5$ groups of neighboring $\text{Hg}(\text{OTeF}_5)_2$ molecules. Among the secondary contacts, the Hg---O contacts are the strongest. The Te---O (1.842(7) Å) and Te---F (1.819(6)–1.839(6) Å) bond lengths are comparable to those of $\text{Xe}(\text{OTeF}_5)_2$ (1.842(11) and 1.843(11) Å; 1.823(9)–1.855(11) Å).³² An interesting feature of the $\text{Hg}(\text{OTeF}_5)_2$ structure is the *gauche*-conformation adopted by the two $-\text{OTeF}_5$ groups in the solid state, with a dihedral Te---O---Hg---O---Te angle of 53.7(3)°. The *gauche*-conformation is attributed to crystal packing and to the aforementioned Hg---O and Hg---F secondary contacts with adjacent $-\text{OTeF}_5$ groups. This was verified computationally by showing that the calculated gas-phase geometry of the unknown trimeric $[\text{Hg}(\text{OTeF}_5)_2]_3$ molecule, which possesses two long Hg---O contacts (2.737 Å), retains the experimental *gauche*-conformation (Te---O---Hg---O---Te, 55.8°; see Computational Results). In contrast, gas-phase monomeric $\text{Hg}(\text{OTeF}_5)_2$ optimizes to an *anti*-conformation (dihedral Te---O---Hg---O---Te angle, 139.1°).

Another interesting structural feature is the O---Hg---O angle, which deviates significantly from linearity (170.5(4)°) in the crystal structure. The deformation, albeit smaller, is reproduced in the calculated gas-phase structure of $[\text{Hg}(\text{OTeF}_5)_2]_3$ (176.0°) which also reproduced the Hg---O secondary contacts. It is therefore likely that this feature predominantly results from crystal packing in addition to the steric demands of the $-\text{OTeF}_5$ ligands. Moreover, the experimental structure contains additional Hg---F(Te) contacts that may further contribute to a decrease in the O---Hg---O angle owing to their steric demands. These contacts originate from Hg---F(Te) interactions between adjacent $\text{Hg}(\text{OTeF}_5)_2$ units within a chain and approach the Hg(II) atom in a direction opposite to the direction toward which the O---Hg---O angle is bent.

$\text{Hg}(\text{OTeF}_5)_2 \cdot 1.5\text{NgF}_2$ (Ng = Xe, Kr). The coordination complexes, $\text{Hg}(\text{OTeF}_5)_2 \cdot 1.5\text{NgF}_2$ are isomorphous and belong to the $P2_1/n$ space group. The crystal structures of $\text{Hg}(\text{OTeF}_5)_2 \cdot 1.5\text{NgF}_2$ are analogous, containing $\text{Hg}(\text{OTeF}_5)_2$ units that are linked to one another through bridging NgF_2 molecules (Figures S4 and 2). As expected, the $\text{Hg}(\text{OTeF}_5)_2 \cdot 1.5\text{XeF}_2$ complex has a slightly larger unit cell (Table 1), reflecting the larger covalent radius of xenon (1.40 Å) relative to that of krypton (1.16 Å).³³

The mercury coordination spheres of $\text{Hg}(\text{OTeF}_5)_2 \cdot 1.5\text{NgF}_2$ are comparable to that of $\text{Hg}(\text{OTeF}_5)_2$ (vide supra), consisting of very distorted pseudo-octahedra (Figure 3 and Table 3). The $\text{Hg}(\text{OTeF}_5)_2$ units likewise have *gauche*-conformations with Hg---O bonds *trans* to one another. The contacts with mercury include two shorter Hg---F contacts (Xe, 2.606(5) and 2.623(4) Å; Kr, 2.664(3) and 2.675(3) Å) that are *trans* to one another and two slightly longer Hg---F and Hg---O contacts (Xe, 2.701(5) and 2.749(4) Å; Kr, 2.741(3) and 2.725(3) Å, respectively) that are *trans* to one another. The Hg---F contacts originate from the fluorine ligands of three nonequivalent NgF_2 molecules and the Hg---O contact from an oxygen atom of an adjacent $\text{Hg}(\text{OTeF}_5)_2$ group. These contacts are significantly less than the sums of their respective van der Waals radii and indicate significant covalent interactions. The Hg---F and Hg---O contacts within the NgF_2 complexes are shorter and longer, respectively, than those within the chain networks of $\text{Hg}(\text{OTeF}_5)_2$ (Hg---F, 2.810(7) and Hg---O, 2.641(7) Å). These secondary bonding interactions, which are similar to the secondary bonding interactions found in the crystal structure of $\text{Hg}(\text{OTeF}_5)_2$, presumably favor the observed *gauche*-conformation of the $\text{Hg}(\text{OTeF}_5)_2$ unit. Although both structures are similar, the secondary bond distances between mercury and the fluorine atoms of NgF_2 are somewhat shorter in $\text{Hg}(\text{OTeF}_5)_2 \cdot 1.5\text{XeF}_2$ than in the KrF₂ analogue (Table 3), which is consistent with the more polar characters of the Xe---F bonds.³

The Te---F bond lengths (Xe, 1.814(5)–1.845(4) Å; Kr, 1.824(3)–1.848(3) Å) and F---Te---F angles (Xe, 85.5(2)–91.8(2)° and 172.1(2)–173.6(3)°; Kr, 86.2(2)–91.3(2)° and 172.5(1)–174.3(1)°) are comparable in the krypton and xenon analogues and to those of $\text{Hg}(\text{OTeF}_5)_2$ (vide supra). The Hg---O (Xe, 2.015(5) and 2.037(5) Å; Kr, 2.017(3) and 2.029(3) Å) and Te---O (Xe, 1.811(6) and 1.815(5) Å; Kr, 1.819(3) and 1.836(3) Å) bond lengths are all equal (within $\pm 3\sigma$) to those of $\text{Hg}(\text{OTeF}_5)_2$. The effects of NgF_2 coordination to mercury are reflected in the O---Hg---O (Xe, 173.0(2)°; Kr, 173.3(1)°) and Hg---Te---O (Xe, 132.8(3) and 127.2(3)°; Kr, 129.6(2) and 126.5(1)°) angles, which are slightly larger (within $\pm 3\sigma$) than those of $\text{Hg}(\text{OTeF}_5)_2$, and in

Table 2. Experimental Geometrical Parameters for $\text{Hg}(\text{OTeF}_5)_2$ and Calculated Geometrical Parameters for $[\text{Hg}(\text{OTeF}_5)_2]_3$

exptl $\text{Hg}(\text{OTeF}_5)_2^a$		calcd $[\text{Hg}(\text{OTeF}_5)_2]_3^b$	
Bond Lengths (Å)			
Hg ₁ –O ₁	2.016(6)	Hg ₁₆ –O ₂₂	2.008
Te ₁ –O ₁	1.842(7)	Te ₁₇ –O ₂₂	1.865
Te ₁ –F ₁	1.819(6)	Te ₁₇ –F ₁₈	1.832
Te ₁ –F ₂	1.824(6)	Te ₁₇ –F ₂₁	1.839
Te ₁ –F ₃	1.830(6)	Te ₁₇ –F ₂₃	1.848
Te ₁ –F ₄	1.833(6)	Te ₁₇ –F ₁₉	1.837
Te ₁ –F ₅	1.839(6)	Te ₁₇ –F ₂₀	1.855
Hg ₁ ···O _{1A}	2.641(7)	Hg ₁₆ ···O ₁₄	2.737
Hg ₁ ···O _{1C}	2.641(7)	Hg ₁₆ ···O ₃₀	2.737
Hg ₁ ···F _{4D}	2.810(7)		
Hg ₁ ···F _{4H}	2.810(7)		
Bond Angles (°)			
O ₁ –Hg ₁ –O _{1B}	170.5(4)	O ₂₂ –Hg ₁₆ –O ₃₇	176.0
Hg ₁ –O ₁ –Te ₁	124.1(3)	Hg ₁₆ –O ₂₂ –Te ₁₇	122.0
O ₁ –Te ₁ –F ₁	178.3(3)	O ₂₂ –Te ₁₇ –F ₁₈	179.6
O ₁ –Te ₁ –F ₂	91.0(3)	O ₂₂ –Te ₁₇ –F ₂₁	90.2
O ₁ –Te ₁ –F ₃	92.9(3)	O ₂₂ –Te ₁₇ –F ₂₃	91.7
O ₁ –Te ₁ –F ₄	90.7(3)	O ₂₂ –Te ₁₇ –F ₁₉	91.6
O ₁ –Te ₁ –F ₅	91.8(3)	O ₂₂ –Te ₁₇ –F ₂₀	91.6
F ₁ –Te ₁ –F ₂	89.0(3)	F ₁₈ –Te ₁₇ –F ₂₁	89.4
F ₁ –Te ₁ –F ₃	88.8(3)	F ₁₈ –Te ₁₇ –F ₂₃	88.2
F ₁ –Te ₁ –F ₄	87.6(3)	F ₁₈ –Te ₁₇ –F ₁₉	88.5
F ₁ –Te ₁ –F ₅	88.2(3)	F ₁₈ –Te ₁₇ –F ₂₀	88.8
F ₂ –Te ₁ –F ₄	89.7(3)	F ₂₁ –Te ₁₇ –F ₁₉	90.2
F ₄ –Te ₁ –F ₅	89.1(3)	F ₁₉ –Te ₁₇ –F ₂₀	90.5
F ₅ –Te ₁ –F ₃	89.5(3)	F ₂₀ –Te ₁₇ –F ₂₃	88.7
F ₃ –Te ₁ –F ₂	91.5(3)	F ₂₃ –Te ₁₇ –F ₂₁	90.5
F ₂ –Te ₁ –F ₅	177.0(3)	F ₂₁ –Te ₁₇ –F ₂₀	178.0
F ₃ –Te ₁ –F ₄	176.2(3)	F ₂₃ –Te ₁₇ –F ₁₉	176.6
O ₁ –Hg ₁ ···F _{4D}	105.9(3)		
O ₁ –Hg ₁ ···F _{4H}	78.3(3)		
O ₁ –Hg ₁ ···O _{1A}	78.7(3)	O ₂₂ –Hg ₁₆ ···O ₁₄	73.0
O ₁ –Hg ₁ ···O _{1C}	93.8(3)	O ₂₂ –Hg ₁₆ ···O ₃₀	103.8
O _{1A} ···Hg ₁ ···F _{4D}	78.3(3)		
O _{1A} ···Hg ₁ ···F _{4H}	105.9(3)		
O _{1C} ···Hg ₁ ···F _{4H}	155.7(3)		
O _{1A} ···Hg ₁ ···O _{1C}	81.3(3)	O ₁₄ ···Hg ₁₆ ···O ₃₀	79.7
F _{4D} ···Hg ₁ ···F _{4H}	129.6(3)		
Dihedral Angles (°)			
Te ₁ –O ₁ –Hg ₁ –O _{1B} –Te _{1B}	53.7(3)	Te ₁₇ –O ₂₂ –Hg ₁₆ –O ₃₇ –Te ₃₂	55.8

^aAtom labeling scheme corresponds to that used in Figure 1b. ^bCalculated at the PBE1PBE/def2-TVZPP level of theory. Atom labeling scheme corresponds to that used in Figure 6b. Only the parameters associated with the central $\text{Hg}(\text{OTeF}_5)_2$ unit are reported.

the dihedral Te–O–Hg–O–Te angles (Xe, 45.2(5)°; Kr, 50.3(3)°), which are smaller than in $\text{Hg}(\text{OTeF}_5)_2$ (53.7(3)°).

There are two crystallographically inequivalent bridging NgF_2 molecules within the asymmetric units of $\text{Hg}(\text{OTeF}_5)_2 \cdot 1.5\text{NgF}_2$; one Ng atom is positioned on an inversion center, providing two symmetry-equivalent Ng–F bonds (Xe, 1.981(4) Å; Kr, 1.883(3) Å), whereas the other Ng atom is on a general position, giving rise to two symmetry-inequivalent Ng–F bonds (Xe, 1.991(4) and 2.012(4) Å; Kr, 1.897(3) and 1.885(3) Å). The Ng–F bond lengths are equal within $\pm 3\sigma$ to those observed in free NgF_2 (XeF₂, 1.999(4) Å;³ KrF₂, 1.894(5) Å²). The Xe–F bond lengths are comparable to those observed for the bridging XeF₂ molecule in $\text{Cd}(\text{XeF}_2)_4(\text{AsF}_6)_2$ (Xe–F_b, 1.995(5) and 2.017(5) Å)¹⁰ and in $\text{Cd}(\text{XeF}_2)_5(\text{PF}_6)_2$ (Xe–F_b, 1.999(6) and 2.016(6) Å).¹¹ The structure of $\text{Hg}(\text{OTeF}_5)_2 \cdot 1.5\text{KrF}_2$ currently represents the only example

of KrF₂ coordinated to a neutral metal center and of a bridging KrF₂ molecule. The $[\text{BrOF}_2][\text{AsF}_6] \cdot 2\text{KrF}_2$ complex is the only other KrF₂ complex reported to date that has been characterized by X-ray crystallography. The Kr–F bridge bonds of the present complex are shorter than the Kr–F bridge bonds of the terminally coordinated KrF₂ molecules in $[\text{BrOF}_2][\text{AsF}_6] \cdot 2\text{KrF}_2$ (1.943(4) and 1.933(4) Å),¹⁵ indicating that they are more covalent and more weakly coordinated than those of $[\text{BrOF}_2][\text{AsF}_6] \cdot 2\text{KrF}_2$.

Raman Spectroscopy. The low-temperature, solid-state Raman spectra of $\text{Hg}(\text{OTeF}_5)_2$ and $\text{Hg}(\text{OTeF}_5)_2 \cdot 1.5\text{NgF}_2$ (Ng = Xe, Kr) are shown in Figures S1, 4, and 5. Their assignments are listed in abbreviated form in Tables 4–6 and in more detail in Tables S1–S4 along with their experimental and calculated frequencies and intensities.

Table 3. Experimental Geometrical Parameters^a for Hg(OTeF₅)₂·1.5NgF₂ (Ng = Xe, Kr)

	Ng = Xe	Ng = Kr		Ng = Xe	Ng = Kr
Bond Lengths (Å)					
Hg ₁ -O ₁	2.015(5)	2.017(3)	Te ₂ -F ₈	1.828(5)	1.836(3)
Hg ₁ -O ₂	2.037(5)	2.029(3)	Te ₂ -F ₉	1.827(5)	1.836(3)
O ₁ -Te ₁	1.815(5)	1.819(3)	Te ₂ -F ₁₀	1.814(5)	1.824(3)
O ₂ -Te ₂	1.811(6)	1.836(3)	Hg ₁ ...O _{2B}	2.749(4)	2.725(3)
Te ₁ -F ₁	1.827(5)	1.837(3)	Hg ₁ ...F ₁₁	2.606(5)	2.664(3)
Te ₁ -F ₂	1.831(4)	1.839(3)	Hg ₁ ...F ₁₂	2.623(4)	2.675(3)
Te ₁ -F ₃	1.837(4)	1.844(3)	Hg ₁ ...F _{13B}	2.701(5)	2.741(3)
Te ₁ -F ₄	1.841(4)	1.848(3)	Ng ₂ -F ₁₁	1.981(4)	1.883(3)
Te ₁ -F ₅	1.845(4)	1.835(3)	Ng ₂ -F _{11A}	1.981(4)	1.883(3)
Te ₂ -F ₆	1.835(5)	1.838(3)	Ng ₁ -F ₁₂	2.012(4)	1.897(3)
Te ₂ -F ₇	1.822(4)	1.829(3)	Ng ₁ -F ₁₃	1.991(4)	1.885(3)
Bond Angles (°)					
O ₁ -Hg ₁ -O ₂	173.0(2)	173.3(1)	F ₈ -Te ₂ -F ₇	87.0(2)	87.7(1)
Hg ₁ -O ₁ -Te ₁	132.8(3)	129.6(2)	F ₈ -Te ₂ -F ₁₀	86.6(3)	87.1(2)
Hg ₁ -O ₂ -Te ₂	127.2(3)	126.5(1)	F ₉ -Te ₂ -F ₇	90.2(2)	90.1(1)
O ₁ -Te ₁ -F ₁	93.2(2)	93.0(1)	F ₇ -Te ₂ -F ₁₀	91.8(2)	91.3(2)
O ₁ -Te ₁ -F ₂	94.7(2)	94.4(1)	F ₁₀ -Te ₂ -F ₆	90.0(2)	90.1(1)
O ₁ -Te ₁ -F ₃	95.3(2)	95.0(1)	F ₆ -Te ₂ -F ₉	87.5(2)	88.0(1)
O ₁ -Te ₁ -F ₄	91.1(2)	90.6(1)	F ₉ -Te ₂ -F ₁₀	173.6(3)	174.2(2)
O ₁ -Te ₁ -F ₅	176.7(2)	176.8(1)	F ₆ -Te ₂ -F ₇	173.5(2)	174.2(1)
O ₂ -Te ₂ -F ₆	95.0(2)	94.8(1)	F _{11A} -Ng ₂ -F ₁₁	180.0	180.0
O ₂ -Te ₂ -F ₇	91.2(2)	90.8(1)	F ₁₂ -Ng ₁ -F ₁₃	179.4(2)	178.9(1)
O ₂ -Te ₂ -F ₈	178.0(2)	178.5(1)	Ng ₂ -F ₁₁ ...Hg ₁	158.3(3)	150.6(2)
O ₂ -Te ₂ -F ₉	93.4(2)	92.7(1)	Ng ₁ -F ₁₂ ...Hg ₁	119.3(2)	119.5(1)
O ₂ -Te ₂ -F ₁₀	92.7(3)	92.8(2)	O ₁ -Hg ₁ ...F _{13B}	79.7(2)	78.5(1)
F ₅ -Te ₁ -F ₂	86.6(2)	86.4(1)	O ₁ -Hg ₁ ...F ₁₁	99.2(2)	99.4(1)
F ₅ -Te ₁ -F ₃	87.7(2)	88.1(1)	O ₁ -Hg ₁ ...F ₁₂	77.2(2)	75.9(1)
F ₅ -Te ₁ -F ₄	86.0(2)	86.3(1)	O ₂ -Hg ₁ ...F _{13B}	101.1(2)	103.0(1)
F ₅ -Te ₁ -F ₁	85.5(2)	86.2(2)	O ₂ -Hg ₁ ...F ₁₁	84.4(2)	83.0(2)
F ₂ -Te ₁ -F ₄	89.5(2)	90.5(1)	O ₂ -Hg ₁ ...F ₁₂	96.4(3)	98.2(2)
F ₄ -Te ₁ -F ₁	89.8(2)	89.4(1)	O ₁ -Hg ₁ ...O _{2B}	103.3(2)	103.4(1)
F ₁ -Te ₁ -F ₃	89.4(2)	89.1(1)	O _{2B} ...Hg ₁ ...F _{13B}	139.9(2)	139.6(1)
F ₃ -Te ₁ -F ₂	90.4(2)	90.2(1)	O _{2B} ...Hg ₁ ...F ₁₁	77.2(2)	74.2(1)
F ₃ -Te ₁ -F ₄	173.6(2)	174.3(1)	O _{2B} ...Hg ₁ ...F ₁₂	69.8(2)	69.4(1)
F ₁ -Te ₁ -F ₂	172.1(2)	172.5(1)	F ₁₂ ...Hg ₁ ...F ₁₁	144.7(2)	140.8(1)
F ₈ -Te ₂ -F ₉	87.4(2)	87.4(2)	F _{13B} ...Hg ₁ ...F ₁₁	142.5(2)	146.0(1)
F ₈ -Te ₂ -F ₆	86.9(2)	86.7(1)	F _{13B} ...Hg ₁ ...F ₁₂	77.2(2)	72.2(1)
Dihedral Angle (°)					
Te ₁ -O ₁ -Hg ₁ -O ₂ -Te ₂	45.2(5)	50.3(3)			

^aAtom labeling schemes correspond to those used in Figures S4 and 2 for Ng = Xe and Kr, respectively.

Spectral assignments for Hg(OTeF₅)₂ were made by comparison with the calculated frequencies and Raman intensities (Tables 4, S1, and S2) obtained for the energy-minimized, gas-phase geometries of Hg(OTeF₅)₂ (C₂) monomer and the presently unknown trimer, [Hg(OTeF₅)₂]₃ (C₁) (Figure 6). The central Hg(OTeF₅)₂ unit of the trimeric model provides a good approximation of the repeat unit in the chain structure (Figure 1). A similar approach has been successfully used to assign the Raman spectra of the polymeric open chain structures OsO₃F₂³⁴ and MoSF₄³⁵. In another related structure, XeOF₄·XeF₂, the model compounds, 2XeOF₄·XeF₂ and XeOF₄·4XeF₂, have provided good approximations for the local environments of XeF₂ and XeOF₄ and their vibrational assignments.³⁶

The -OTeF₅ ligands of the central Hg(OTeF₅)₂ unit of [Hg(OTeF₅)₂]₃ have a *gauche*-conformation and two *cis*-Hg...O secondary contacts to the Hg(II) atoms from the terminal Hg(OTeF₅)₂ units. The Raman spectrum of Hg-

(OTeF₅)₂ is also compared with that of Xe(OTeF₅)₂.³² The vibrational assignments for Hg(OTeF₅)₂·1.5NgF₂ were made by comparison with the experimental frequencies of Hg(OTeF₅)₂ (Table 4) and NgF₂ (Tables S5 and S6), and the calculated frequencies and assignments of NgF₂ (Tables S5 and S6) and the [Hg(OTeF₅)₂]₃·2NgF₂ model compounds. These models enabled the assignments of the intramolecular coupled modes that occur among Hg(OTeF₅)₂ units and/or NgF₂ units. The following frequency assignments and related discussions exclusively refer to the modes associated with the central Hg(OTeF₅)₂ units of gas-phase [Hg(OTeF₅)₂]₃ and [Hg(OTeF₅)₂]₃·2NgF₂ and with the NgF₂ ligands. The calculated frequencies of $\nu_{as}(\text{NgF}_2)$, $\nu_s(\text{NgF}_2)$, and $\delta(\text{KrF}_2)$ of free XeF₂ and KrF₂ were overestimated, whereas that of $\delta(\text{XeF}_2)$ was close to the experimental value (Tables S5 and S6). This pattern aided in the assignment of the corresponding calculated frequencies of the [Hg(OTeF₅)₂]₃·2NgF₂ complexes.

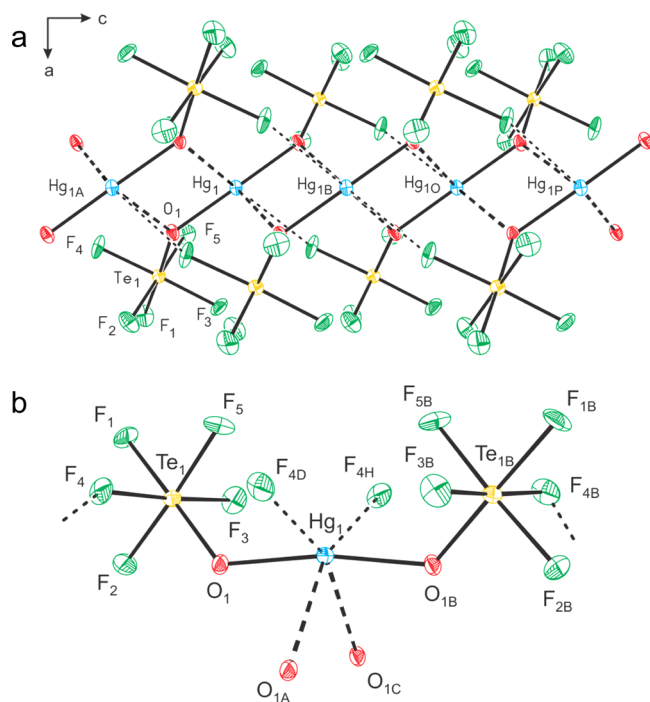


Figure 1. The X-ray crystal structure of $\text{Hg}(\text{OTeF}_5)_2$ showing (a) its chain structure viewed along the b -axis and running parallel to the c -axis and (b) the pseudo-octahedral coordination around $\text{Hg}(\text{II})$ resulting from the secondary bonding interactions (indicated by dashed lines) between $\text{Hg}(\text{II})$ and the F and O atoms of $-\text{OTeF}_5$ groups in adjacent $\text{Hg}(\text{OTeF}_5)_2$ units; thermal ellipsoids are shown at the 50% probability level.

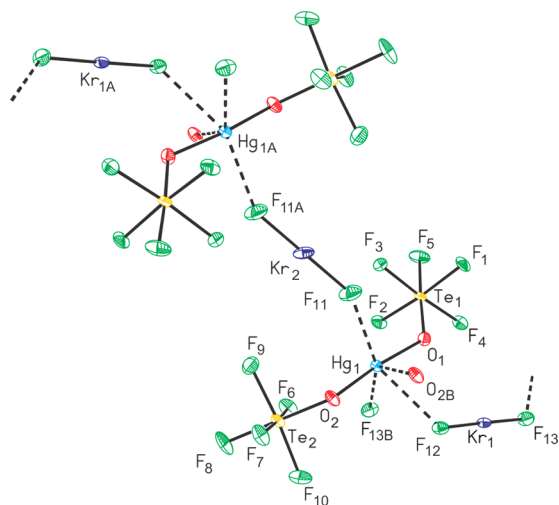


Figure 2. The chain structure in the X-ray crystal structure of $\text{Hg}(\text{OTeF}_5)_2 \cdot 1.5\text{KrF}_2$; thermal ellipsoids are shown at the 50% probability level. Secondary bonding interactions from the F and O atoms of adjacent KrF_2 and $-\text{OTeF}_5$ groups to $\text{Hg}(\text{II})$ are indicated by dashed lines.

$\text{Hg}(\text{OTeF}_5)_2$. The vibrational assignments of $\text{Hg}(\text{OTeF}_5)_2$ were initially based on a gas-phase monomeric model (C_2 symmetry, Table S1, and Figure 6a). The 39 vibrations of monomeric $\text{Hg}(\text{OTeF}_5)_2$ span the irreducible representations $\Gamma_{\text{vib}} = 20\text{A} + 19\text{B}$, which are Raman and infrared active.

The calculated vibrational frequencies and intensities at the B3LYP and PBE1PBE levels of theory using the def2-TZPP and aug-cc-PTVZ basis sets reproduce the experimental trends,

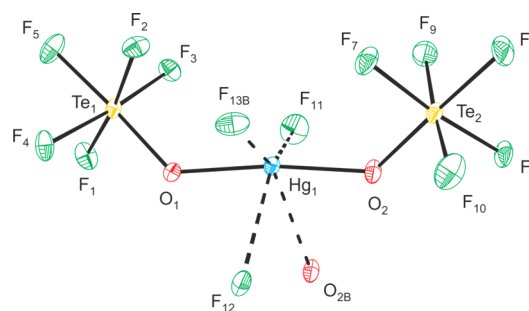


Figure 3. The structural unit in the X-ray crystal structure of $\text{Hg}(\text{OTeF}_5)_2 \cdot 1.5\text{KrF}_2$ (see Figure 2) with thermal ellipsoids drawn at the 50% probability level. Secondary bonding interactions are indicated by dashed lines drawn from the F and O atoms of adjacent KrF_2 and $-\text{OTeF}_5$ groups to $\text{Hg}(\text{II})$ and show the pseudo-octahedral coordination around $\text{Hg}(\text{II})$.

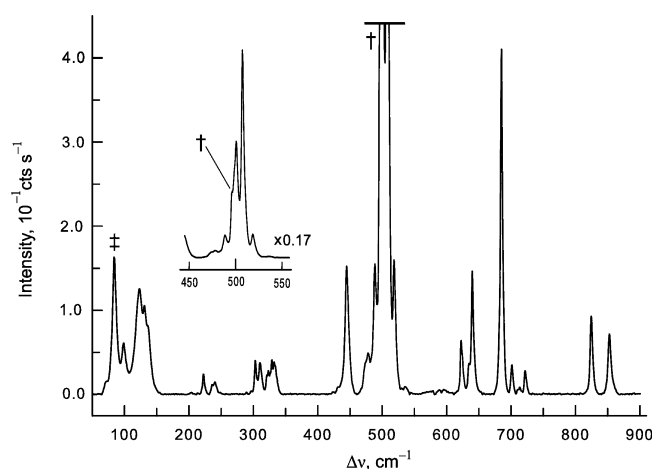


Figure 4. The Raman spectrum of $\text{Hg}(\text{OTeF}_5)_2 \cdot 1.5\text{XeF}_2$ recorded in a quartz tube at -155°C using 1064-nm excitation. Symbols denote unreacted XeF_2 at 496 cm^{-1} (\dagger) and an instrumental artifact (\ddagger).

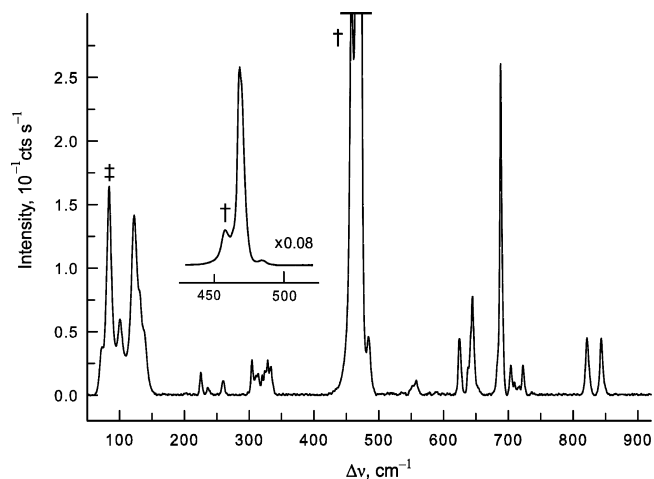


Figure 5. The Raman spectrum of $\text{Hg}(\text{OTeF}_5)_2 \cdot 1.5\text{KrF}_2$ recorded in a quartz tube at -155°C using 1064-nm excitation. Symbols denote unreacted KrF_2 at 464 cm^{-1} (\dagger) and an instrumental artifact (\ddagger).

but the $\text{Hg}(\text{OTeF}_5)_2$ frequencies obtained at the B3LYP level (Table S1) were significantly underestimated when compared with the frequencies calculated at the PBE1PBE level. Consequently, calculations for $[\text{Hg}(\text{OTeF}_5)_2]_3$ and $[\text{Hg}(\text{OTeF}_5)_2]_3 \cdot 2\text{NgF}_2$ were carried out at the PBE1PBE

Table 4. Experimental Raman Frequencies and Intensities for $\text{Hg}(\text{OTeF}_5)_2$ and Calculated Vibrational Frequencies and Intensities for $[\text{Hg}(\text{OTeF}_5)_2]_3$

exptl ^{a,b,c}		calcd ^{a,d}	
$\text{Hg}(\text{OTeF}_5)_2$		$[\text{Hg}(\text{OTeF}_5)_2]_3$	
assgnmts ^e			
825(19)	824(27)[76]	}	[$\nu(\text{Hg-O}) - \nu(\text{Te-O})$]
n.o.	806(4)[112]		
801(8)	793(3)[663]		
	787(1)[314]	}	[$\nu(\text{Te-F}_c)$]
735(25)	726(11)[2]		
	725(<0.1)[218]		
	724(<0.1)[235]	}	[$\nu(\text{Te-F}_a)$]
709(100)	709(6)[45]		
	707(28)[61]		
	719(15)[<1]	}	[$\nu(\text{Te-F}_c)$]
699(3)	719(<1)[392]		
	717(<1)[17]		
	716(<1)[249]	}	[$\nu(\text{Hg-O}) + \nu(\text{Te-O})$]
652(46)	714(2)[18]		
	654(50)[1]		
647, sh	649(1)[10]	}	[$\nu(\text{Hg-O}) + \nu(\text{Te-O})$]
630, sh	649(<1)[10]		
624(45)	641(2)[8]		
	640(6)[<1]	}	[$\nu(\text{Hg-O}) + \nu(\text{Te-O})$]
511(7)	530(2)[81]		
	528(6)[11]		
481(52)	506(75)[3]	}	[$\nu(\text{Hg-O}) + \nu(\text{Te-O})$]
472, sh	516(3)[138]		
349(2)	341(<1)[5]		
	332(<0.1)[137]	}	$\delta(\text{TeF}_{4e})_{\text{umb}}$
331(9)	331(<0.1)[219]		
	328(<0.1)[364]		
327(20)	327(<1)[22]	}	$\delta(\text{O-Hg-O})_{\text{o.o.p.}}$
	324(<0.1)[52]		
324, sh	323(<1)[15]		
	320(2)[17]	}	$\delta(\text{TeF}_{4e})_{\text{umb}}$
318(5)	320(<0.1)[11]		
	315(6)[1]		
	315(<1)[<0.1]	}	$\delta(\text{O-Hg-O})_{\text{o.o.p.}}$
312(1)	315(<1)[<0.1]		
	295(2)[<1]		
298(9)	295(1)[<0.1]	}	$\delta(\text{F-Te-F})$
	245(<1)[<1]		
n.o.	244(<0.1)[4]		
	234(<0.1)[7]	}	$\rho_w(\text{F-Te-F})$
233(12)	232(6)[1]		
	207(<0.1)[<1]		
	206(<0.1)[<0.1]	}	$\delta(\text{F-Te-F}) / \rho_w(\text{F-Te-F})$
n.o.	195(<0.1)[<0.1]		
	191(<0.1)[<0.1]		
194(2)	190(<1)[<0.1]	}	$\delta(\text{F-Te-F}) / \rho_w(\text{F-Te-F})$
173(<1)	167(<0.1)[<1]		
	129(<1)[2]		
127(16)	127(4)[<0.1]	}	$\rho_w(\text{F-Te-F}) / \delta(\text{O-Hg-O})_{\text{o.o.p.}}$
	97(<1)[17]		
92(9)	94(<0.1)[3]		
	93(2)[1]	}	$\rho_w(\text{F-Te-F}) / \delta(\text{O-Hg-O})_{\text{o.o.p.}}$

^aFrequencies are given in cm^{-1} . ^bValues in parentheses denote relative Raman intensities. The Raman spectrum was recorded in an FEP sample tube at -150°C using 1064-nm excitation. ^cThe abbreviations denote shoulder (sh) and not observed (n.o.). ^dValues in parentheses denote calculated Raman intensities ($\text{\AA}^4 \text{amu}^{-1}$), whereas values in square brackets denote calculated infrared intensities (km mol^{-1}). ^eAssignments are for the energy-minimized geometry calculated at the PBE1PBE/def2-TZVPP level; only simplified mode assignments (separated by the symbol “/”) that involve the central $\text{Hg}(\text{OTeF}_5)_2$ unit are listed. See Table S2 for a complete listing of frequencies and detailed descriptions of the assignments. The abbreviations denote out-of-plane (o.o.p.) and in-plane (i.p.) where the planes contain the (Te–O–Hg–O–Te) groups, umbrella (umb), equatorial (e), axial (a), stretch (ν), bend (δ), twist (ρ_t), wag (ρ_w), and rock (ρ_r). The atom labeling scheme is given in Figures 6b and S5.

level using only the def2-TZPP basis set due to the large sizes of these molecules. Although most of the observed frequencies and intensities could be accounted for using the gas-phase monomeric model, the observation of additional bands that are

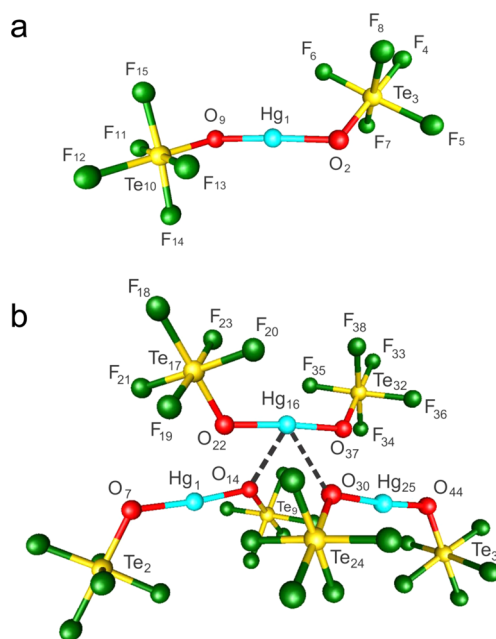


Figure 6. The gas-phase, energy-minimized geometries of (a) monomeric $\text{Hg}(\text{OTeF}_5)_2$ (C_2) and (b) trimeric $[\text{Hg}(\text{OTeF}_5)_2]_3$ (C_1) calculated at the PBE1PBE/def2-TZVPP level of theory. The long contacts (dashed lines) between the Hg(II) atom of the central $\text{Hg}(\text{OTeF}_5)_2$ unit and two oxygen atoms of two adjacent terminal $\text{Hg}(\text{OTeF}_5)_2$ units are shown in (b).

not accounted for by the monomeric model suggested that this model was too limited. Moreover, the *anti*-conformation of the $-\text{OTeF}_5$ groups in the gas-phase monomer differs from that of the solid-state *gauche*-conformation.

The use of the trimeric model, $[\text{Hg}(\text{OTeF}_5)_2]_3$, (Figure 6b) addresses these differences by reproducing the *gauche*-conformation and revealing that the additional bands that were not accounted for in the monomeric model arise from intermolecular couplings among its $\text{Hg}(\text{OTeF}_5)_2$ units (see above and Tables 4 and S2).

The $\nu(\text{Hg-O})$ and $\nu(\text{Te-O})$ stretches couple, giving rise to eight vibrational modes. Four of these modes are derived from “symmetric” [$\nu(\text{Hg-O}) + \nu(\text{Te-O})$]-type stretching modes. The [$\nu(\text{Hg}_{16}-\text{O}_{22}) + \nu(\text{Te}_{17}-\text{O}_{22})$] mode is in-phase coupled to [$\nu(\text{Hg}_{16}-\text{O}_{37}) + \nu(\text{Te}_{32}-\text{O}_{37})$] and is also coupled in-phase (481 cm^{-1}) and out-of-phase (472 cm^{-1}) with the analogous modes of the two outer $\text{Hg}(\text{OTeF}_5)_2$ units of the trimer. The totally in-phase coupled mode at 481 cm^{-1} is the second most intense band in the spectrum. The calculated frequencies (506 and 516 cm^{-1} , respectively) are in good agreement with the observed values. As in the experimental spectrum, the calculated Raman intensity of the 506 cm^{-1} band is also very intense. The [$\nu(\text{Hg}_{16}-\text{O}_{22}) + \nu(\text{Te}_{17}-\text{O}_{22})$] mode is also out-of-phase coupled to the [$\nu(\text{Hg}_{16}-\text{O}_{37}) + \nu(\text{Te}_{32}-\text{O}_{37})$] mode (511 cm^{-1}). The [$\nu(\text{Hg}_{16}-\text{O}_{22}) + \nu(\text{Te}_{17}-\text{O}_{22})$] mode is further coupled in-phase and out-of-phase (530 cm^{-1}) and out-of-phase and in-phase (528 cm^{-1}) to the analogous modes of the two terminal $\text{Hg}(\text{OTeF}_5)_2$ units. The agreement between the observed (511 cm^{-1}) and calculated values (530 and 528 cm^{-1}) is again very good. Four modes are predicted which involve the “asymmetric” [$\nu(\text{Hg}_{16}-\text{O}_{22}) - \nu(\text{Te}_{17}-\text{O}_{22})$] and [$\nu(\text{Hg}_{16}-\text{O}_{37}) - \nu(\text{Te}_{32}-\text{O}_{37})$] stretching modes and are expected to be out-of-phase (793 cm^{-1}) and in-phase (787 , 806 , and 824 cm^{-1}) coupled. The latter three modes arise from

Table 5. Experimental Raman Frequencies and Intensities for $\text{Hg}(\text{OTeF}_5)_2 \cdot 1.5\text{XeF}_2$ and Calculated Vibrational Frequencies and Intensities for $[\text{Hg}(\text{OTeF}_5)_2]_3 \cdot 2\text{XeF}_2$

exptl ^{a,b,c}		calcd ^{a,d}	
$\text{Hg}(\text{OTeF}_5)_2 \cdot 1.5\text{XeF}_2$		$[\text{Hg}(\text{OTeF}_5)_2]_3 \cdot 2\text{XeF}_2$	
		assgnts ^e	
853(5)	828(9)[155]	}	[v(Hg-O) – v(Te-O)]
825(7)	817(2)[547]		
	815(2)[346]		
753(<1) _{broad}	721(16)[10]	}	[v(Te-F _e)]
	717(4)[102]		
	716(5)[291]		
722(2)	715(9)[278]		
711(<1)	714(2)[135]		
	713(2)[13]	}	[v(Te-F _a)]
	713(2)[243]		
	711(<1)[21]	}	[v(Te-F _e)]
702(3)	695(<1)[205]		
	705(13)[8]	}	[v(Te-F _a)]
685(29)	699(18)[18]		
	644(38)[4]	}	[v(Te-F _e)]
640(10)	643(2)[11]		
635(2)	640(3)[8]		
	639(3)[7]	}	[v(Te-F _e)]
623(4)	628(9)[14]		
	622(3)[14]	}	[v(Xe ₁₃ -F ₁₇) – v(Xe ₁₃ -F ₂₀)] / [v(Hg-O) + v(Te-O)]
518(10)	534(3)[178]		
	528(5)[167]	}	[v(Xe ₁₆ -F ₂₃) – v(Xe ₁₆ -F ₄₀)] / [v(Hg-O) + v(Te-O)]
	524(9)[67]		
508(100)	521(54)[90]	}	[v(Xe ₁₃ -F ₂₀) – v(Xe ₁₆ -F ₄₀)]
	516(38)[11]		
501(56)	510(35)[80]	}	[v(Xe ₁₃ -F ₁₇) + v(Xe ₁₃ -F ₂₀)] + [v(Xe ₁₆ -F ₂₃) + v(Xe ₁₆ -F ₄₀)] _{small}
489(10)	510(35)[80]		
478(3)	502(73)[3]	}	[v(Hg-O) + v(Te-O)]
474, sh			
445(11)	499(6)[230]	}	[v(Hg-O) + v(Te-O)] / v(Xe ₁₆ -F ₂₃)
	337(<1)[34]		
334, sh	334(<1)[10]	}	$\delta(\text{TeF}_{4e})_{\text{umb}}$
	334(<1)[99]		
	331(<1)[95]		
332(3)	330(<1)[83]	}	$\delta(\text{O-Hg-O})_{\text{o.o.p.}} / \delta(\text{TeF}_{4e})_{\text{umb}}$
	328(1)[145]		
329(3)	326(<1)[54]	}	$\delta(\text{O-Te-F}) / \delta(\text{F-Te-F}) / \rho_w(\text{F-Te-F})$
	326(<1)[34]		
326, sh	326(1)[21]	}	$\delta(\text{O-Hg-O})_{\text{o.o.p.}} / \delta(\text{O-Te-F}) / \delta(\text{F-Te-F}) / \rho_w(\text{O-Te-F}) / \rho_w(\text{F-Te-F})$
	324(<1)[13]		
324(2)	322(<1)[28]	}	$\delta(\text{F-Te-F}) / \rho_w(\text{F-Te-F}) / \delta(\text{F-Te-F})$
	321(<1)[8]		
321(1)	320(<1)[26]	}	$\delta(\text{F-Te-F}) / \rho_w(\text{F-Te-F})$
	317(<1)[12]		
	316(1)[16]	}	$\rho_i(\text{O-Hg-O}) / \delta(\text{F-Te-O}) / \delta(\text{F-Te-F})$
311(2)	316(<1)[15]		
	293(2)[<1]	}	$\delta(\text{F-Te-F})$
303(3)	291(1)[<1]		
248, sh	244(<1)[<1]	}	$\delta(\text{F-Te-O}) / \rho_w(\text{F-Te-F})$
241(1)	236(<1)[22]		
236(1)	231(3)[3]	}	$\rho_w(\text{F-Te-F}) / \delta(\text{F-Te-O})$
	221(<1)[21]		
223(2)	219(<1)[21]	}	$[\delta(\text{F}_{17}\text{-Xe}_{13}\text{-F}_{20})_{\text{i.p.}}]_{\text{small}} + \delta(\text{F}_{23}\text{-Xe}_{16}\text{-F}_{40})_{\text{o.o.p.}}$
	218(<0.1)[12]		
	210(<0.1)[<1]	}	$\delta(\text{F}_{17}\text{-Xe}_{13}\text{-F}_{20})_{\text{i.p.}} + [\delta(\text{F}_{23}\text{-Xe}_{16}\text{-F}_{40})_{\text{o.o.p.}}]_{\text{small}}$
	209(<0.1)[<1]		
	202(<0.1)[<1]	}	$\rho_w(\text{F-Te-F})$
n.o.	191(<0.1)[<0.1]		
	162(<0.1)[6]	}	$\rho_w(\text{O-Te-F}) / \rho_w(\text{F-Te-F})$
	129(1)[<1]		
137(5)	128(2)[<1]	}	$\rho_i(\text{TeF}_{2e}\text{F}_a)$
131(7)	106(4)[9]		
124(8)	100(<1)[3]	}	$\rho_i(\text{F}_{17}\text{-Xe}_{13}\text{-F}_{20})$
	96(1)[3]		
	91(<1)[5]	}	$\rho_i(\text{F}_{17}\text{-Xe}_{13}\text{-F}_{20}) / \delta(\text{O-Hg-O})_{\text{i.p.}}$
99(3)	83(2)[<1]		
	78(3)[<1]	}	$\delta(\text{O-Hg-O})_{\text{o.o.p.}} / \rho_i(\text{F}_{20}\text{-Xe}_{13}\text{-F}_{17})_{\text{small}}$
	72(2)[<1]		
		}	$\delta(\text{O-Hg-O})_{\text{o.o.p.}} / \rho_i(\text{F}_{20}\text{-Xe}_{13}\text{-F}_{17})_{\text{small}}$
		}	$\rho_i(\text{F}_{40}\text{-Xe}_{16}\text{-F}_{23})$
		}	$\rho_i(\text{F}_{40}\text{-Xe}_{16}\text{-F}_{23})$
		}	$\rho_i(\text{F}_{17}\text{-Xe}_{13}\text{-F}_{20})$

^aFrequencies are given in cm^{-1} . ^bValues in parentheses denote relative Raman intensities. The Raman spectrum was recorded in a quartz sample tube at $-155\text{ }^\circ\text{C}$ using 1064-nm excitation. A band at $496(27)\text{ cm}^{-1}$ (not listed, see Figure 4) is assigned to excess XeF_2 . ^cThe abbreviations denote shoulder (sh) and not observed (n.o.). ^dValues in parentheses denote calculated Raman intensities ($\text{\AA}^4\text{ amu}^{-1}$), whereas values in square brackets denote calculated infrared intensities (km mol^{-1}). ^eAssignments are for the energy-minimized geometry calculated at the PBE1PBE/def2-TZVPP level. Only simplified mode assignments (separated by the symbol “/”) that involve the central $\text{Hg}(\text{OTeF}_5)_2$ unit are listed; the modes involving XeF_2 are fully described. See Table S3 for a complete listing of frequencies and more detailed descriptions of the assignments. The abbreviations denote out-of-plane (o.o.p.) and in-plane (i.p.) where the planes may contain the (Te–O–Hg–O–Te) groups or the two XeF_2 molecules, umbrella (umb), equatorial (e), axial (a), stretch (ν), bend (δ), twist (ρ_t), wag (ρ_w), and rock (ρ_r). The subscript “small” denotes that the bracketed vibrational mode makes a small contribution relative to the other coupled vibrations. The atom labeling scheme is given in Figure S6a.

Table 6. Experimental Raman Frequencies and Intensities for $\text{Hg}(\text{OTeF}_5)_2 \cdot 1.5\text{KrF}_2$ and Calculated Vibrational Frequencies and Intensities for $[\text{Hg}(\text{OTeF}_5)_2]_3 \cdot 2\text{KrF}_2$

exptl ^{a,b,c}		calcd ^{d,e}			
$\text{Hg}(\text{OTeF}_5)_2 \cdot 1.5\text{KrF}_2$		$[\text{Hg}(\text{OTeF}_5)_2]_3 \cdot 2\text{KrF}_2$			
		assgnts ^e			
844(3)	826(9)[165]	}	[v(Hg-O) - v(Te-O)]		
821(2)	812(2)[358]				
723(1)	723(16)[15]				
717(<1)	718(4)[92]	}	[v(Te-F _e)]		
	717(5)[294]				
	715(13)[215]				
	715(2)[186]				
	714(1)[32]				
709(1)	713(2)[195]	}	[v(Te-F _a)]		
704(1)	712(<1)[49]				
688(14)	693(1)[231]	}	[v(Te-F _e)]		
	706(12)[7]				
	700(2)[223]				
683, sh	699(20)[4]	}	[v(Te-F _e)]		
645(4)	646(24)[12]				
	642, sh			642(3)[8]	
638(1)	641(2)[9]			}	[v(Te-F _e)]
624(2)	627(11)[22]				
558(1)	624(2)[32]	}	[v(Te-F _e)]		
553(<1)	623(4)[3]				
484(3)	574(2)[342]	}	[v(Kr ₁₃ -F ₁₇) - v(Kr ₁₃ -F ₂₀)] + [v(Kr ₁₆ -F ₂₃) - v(Kr ₁₆ -F ₄₀)]		
	553(<1)			560(6)[339]	
	484(3)			527(2)[34]	
468(100)	513(61)[5]	}	[v(Kr ₁₃ -F ₁₇) + v(Kr ₁₃ -F ₂₀)] + [v(Kr ₁₆ -F ₂₃) + v(Kr ₁₆ -F ₄₀)]		
	458(17)			512(100)[5]	
334(1)	505(69)[37]	}	[v(Hg-O) + v(Te-O)]		
	337(<1)[35]				
	335(<1)[14]				
329(1)	334(<1)[102]	}	$\delta(\text{TeF}_{4e})_{\text{umb}}$		
	331(<1)[62]				
	330(<1)[102]				
324(1)	328(1)[133]	}	$\delta(\text{O-Hg-O})_{\text{o.o.p.}} / \delta(\text{TeF}_{4e})_{\text{umb}}$		
	326(<1)[70]				
	326(<1)[22]				
	326(1)[62]				
320(1)	322(<1)[25]	}	$\delta(\text{O-Te-F}) / \delta(\text{F-Te-F}) / \rho_w(\text{F-Te-F})$		
	321(<1)[19]				
	320(<1)[22]				
	320(2)[21]				
	316(1)[20]				
311(1)	316(<1)[18]	}	$\delta(\text{O-Te-F}) / \delta(\text{F-Te-F}) / \rho_w(\text{F-Te-F})$		
304(2)	293(2)[<1]				
291, sh	291(1)[<1]	}	$\delta(\text{F-Te-F})$		
260(1)	266(<1)[25]				
237(<1)	254(<1)[18]	}	$\delta(\text{F}_{17}\text{-Kr}_{13}\text{-F}_{20})_{\text{o.o.p.}}$		
	252(1)[22]				
	252(<1)[10]				
	244(<1)[5]				
n.o.	243(<1)[3]	}	$\delta(\text{F}_{17}\text{-Kr}_{13}\text{-F}_{20})_{\text{i.p.}} / \delta(\text{F-Te-F}) / \rho_w(\text{F-Te-F})$		
225(1)	231(3)[4]				
n.o.	211(<0.1)[<1]	}	$\rho_w(\text{F-Te-F})$		
n.o.	209(<0.1)[<1]				
n.o.	192(<1)[<1]	}	$\rho_w(\text{O-Te-F}) / \rho_w(\text{F-Te-F})$		
n.o.	161(<0.1)[6]				
138, sh	129(2)[<1]	}	$\rho_t(\text{TeF}_{2e}) / \rho_w(\text{F-Te-F})$		
130, sh	102(2)[7]				
123(7)	98(2)[3]	}	$\rho_t(\text{F}_{20}\text{-Kr}_{13}\text{-F}_{17}) + \rho_t(\text{Te}_{33}\text{-F}_{3,4,5}) - \rho_t(\text{Te}_6\text{-F}_9, \text{F}_{10}, \text{F}_{11})$		
101(3)	95(4)[4]				
n.o.	94(1)[2]	}	$\rho_t(\text{F}_{20}\text{-Kr}_{13}\text{-F}_{17}) / \rho_t(\text{TeF}_{2e})$		
	91(1)[5]				
	78(3)[2]				
	77(7)[<1]				
	70(2)[1]				
67(<1)[1]	67(<1)[1]	}	$\delta(\text{O-Hg-O})_{\text{o.o.p.}} / \rho_t(\text{F}_{20}\text{-Kr}_{13}\text{-F}_{17})_{\text{small}}$		

^aFrequencies are given in cm^{-1} . ^bValues in parentheses denote relative Raman intensities. The Raman spectrum was recorded in a quartz sample tube at $-155\text{ }^\circ\text{C}$ using 1064-nm excitation. The band at $464(21)\text{ cm}^{-1}$ (not listed, see Figure 5) is assigned to excess KrF_2 . ^cThe abbreviations denote shoulder (sh) and not observed (n.o.). ^dValues in parentheses denote calculated Raman intensities ($\text{\AA}^4\text{ amu}^{-1}$), whereas values in square brackets denote calculated infrared intensities (km mol^{-1}). ^eAssignments are for the energy-minimized geometry calculated at the PBE1PBE/def2-TZVPP level. Only simplified mode assignments (separated by the symbol “/”) that involve the central $\text{Hg}(\text{OTeF}_5)_2$ unit are listed; the modes involving KrF_2 are fully described. See Table S4 for a complete listing of frequencies and more detailed descriptions of the assignments. The abbreviations denote out-of-plane (o.o.p.) and in-plane (i.p.) where the planes may contain the (Te-O-Hg-O-Te) groups or the two KrF_2 molecules, umbrella (umb), equatorial (e), axial (a), stretch (ν), bend (δ), twist (ρ_t), wag (ρ_w) and rock (ρ_r) modes. The subscript “small” denotes that the bracketed vibrational mode makes a small contribution relative to the other coupled vibrations. The atom labeling scheme is given in Figures 7 and S6b.

additional coupling with the analogous modes of the terminal $\text{Hg}(\text{OTeF}_5)_2$ units. The calculated band at 824 cm^{-1} is expected to be relatively intense and is observed as a medium-intensity band at 825 cm^{-1} . The weak Raman band at 801 cm^{-1} has been assigned to the weak modes calculated at 793 and 787 cm^{-1} . The calculated mode at 806 cm^{-1} was not observed and is predicted to be weak in the Raman spectrum.

The above frequencies and relative intensities are reminiscent of, but are at higher frequency than those observed for the coupled $\nu(\text{Xe}-\text{O})$ and $\nu(\text{Te}-\text{O})$ stretches in $\text{Xe}(\text{OTeF}_5)_2$ ($440/445$, $796/788$, and 730 cm^{-1}).³² The band analogous to the low-intensity band of $\text{Hg}(\text{OTeF}_5)_2$ at 511 cm^{-1} is predicted at 547 cm^{-1} in $\text{Xe}(\text{OTeF}_5)_2$, i.e., $[\nu(\text{Xe}-\text{O}) + \nu(\text{Te}-\text{O})] - [\nu(\text{Xe}-\text{O}') - \nu(\text{Te}'-\text{O}')] + \delta(\text{OXeO}')$, but was not observed.³² The $\text{O}_{22}-\text{Hg}_{16}-\text{O}_{37}$ bending mode of $\text{Hg}(\text{OTeF}_5)_2$ is observed as a weak band at 331 cm^{-1} (calcd, 332 cm^{-1}), and its frequency is very similar to that of $\delta(\text{O}-\text{Xe}-\text{O})$ (328 cm^{-1}) in $\text{Xe}(\text{OTeF}_5)_2$.³²

The bands between 624 and 735 cm^{-1} are assigned to stretching modes of the TeF_5 groups and are in good agreement with the calculated values ($640-726\text{ cm}^{-1}$) and with those observed in $\text{Xe}(\text{OTeF}_5)_2$ ($635-710\text{ cm}^{-1}$).³² In both cases, the coupled axial $\nu_s(\text{Te}-\text{F}_a)$ modes occur as strong bands in the Raman spectrum ($\text{Hg}(\text{OTeF}_5)_2$, 709 cm^{-1} ; $\text{Xe}(\text{OTeF}_5)_2$, 690 cm^{-1}). The coupled umbrella mode, $[\delta(\text{Te}_{17}\text{F}_{4e})_{\text{umb}} + \delta(\text{Te}_{32}\text{F}_{4e})_{\text{umb}}]$, is observed as a weak band at 349 cm^{-1} (calcd, 341 cm^{-1}) that also in-phase couples with the analogous modes of the two outer $\text{Hg}(\text{OTeF}_5)_2$ units. This mode was not observed for $\text{Xe}(\text{OTeF}_5)_2$ (calcd, 360 cm^{-1}).³²

$\text{Hg}(\text{OTeF}_5)_2 \cdot 1.5\text{NgF}_2$. Spectral assignments were aided by obtaining the energy-minimized geometries of the unknown model complexes, $[\text{Hg}(\text{OTeF}_5)_2]_3 \cdot 2\text{NgF}_2$, and their vibrational frequencies at the PBE1PBE level using the def2-TZPP basis set (Tables S, 6, S3, and S4). These approximations reliably reproduced the experimental trends. Overall, couplings among the vibrational modes of the XeF_2 complex are more extensive than among the vibrational modes of the KrF_2 complex.

As observed for $[\text{Hg}(\text{OTeF}_5)_3]_3$, the two highest frequency bands (Xe, 853 and 825 cm^{-1} ; Kr, 844 and 821 cm^{-1}) involve “asymmetric” $[\nu(\text{Hg}_{12}-\text{O}_{28}) - \nu(\text{Te}_{14}-\text{O}_{28})]$ and $[\nu(\text{Hg}_{12}-\text{O}_{31}) - \nu(\text{Te}_{15}-\text{O}_{31})]$ stretches which are in-phase and out-of-phase coupled. These bands are shifted to higher frequencies relative to the analogous Raman bands of solid $\text{Hg}(\text{OTeF}_5)_2$ (825 and 801 cm^{-1}), a trend that is also observed for the calculated frequencies (Xe, 828 and $817/815\text{ cm}^{-1}$; Kr, 826 and 812 cm^{-1} ; $[\text{Hg}(\text{OTeF}_5)_2]_3$, $824/806$ and $787/793\text{ cm}^{-1}$). These shifts are noteworthy because the experimental Hg–O and Te–O bond lengths are equal within $\pm 3\sigma$ in the crystal structures of $\text{Hg}(\text{OTeF}_5)_2$ and $\text{Hg}(\text{OTeF}_5)_2 \cdot 1.5\text{NgF}_2$. As observed in earlier studies, the present studies also illustrate that Raman spectroscopy can be a more sensitive probe than X-ray crystallography for the detection of small bond strength/bond length differences. The high-frequency shifts of the XeF_2 adduct are anticipated because the Hg–F(NgF) contacts are shorter in the XeF_2 complex ($2.606(5)$ and $2.623(4)\text{ \AA}$) than in the KrF_2 complex ($2.664(3)$ and $2.675(3)\text{ \AA}$) (see X-ray crystallography). The experimental stretching frequencies of the axial fluorine atoms are also affected, shifting to lower frequency (Xe, 685 cm^{-1} ; Kr, 683 and 688 cm^{-1}) relative to $\text{Hg}(\text{OTeF}_5)_2$ (709 cm^{-1}). The corresponding calculated frequencies also follow the same trend (Xe: 699 , 705 cm^{-1} ; Kr: 699 , 700 , 706 cm^{-1} ; $[\text{Hg}(\text{OTeF}_5)_2]_3$: 707 , 709 cm^{-1}). Bands involving $\nu(\text{Te}-\text{F}_e)$ stretches are not predicted to be

significantly affected by complex formation (see X-ray Crystallography); moreover, the Te–F_e bond lengths are equal within $\pm 3\sigma$ among all crystal structures. In practice, these bands show very little, if any, change among the complexes and $\text{Hg}(\text{OTeF}_5)_2$ (Xe: $702-753$, $623-640\text{ cm}^{-1}$; Kr: $704-723$, $624-645\text{ cm}^{-1}$; $\text{Hg}(\text{OTeF}_5)_2$: 735 , $624-699\text{ cm}^{-1}$). The calculated frequencies also remain within the same ranges (Xe: $695-721$, $622-644\text{ cm}^{-1}$; Kr: $693-723$, $623-646\text{ cm}^{-1}$; $[\text{Hg}(\text{OTeF}_5)_2]_3$: $724-726$, $640-719\text{ cm}^{-1}$). The frequencies of the $\delta(\text{TeF}_{4e})_{\text{umb}}$ umbrella modes also remain essentially unchanged. The bands below 332 (Xe) and 329 cm^{-1} (Kr) are assigned to coupled deformation and torsional modes and are well reproduced by the calculations (Tables S and 6). Modes that are exclusively of the “symmetric” $[\nu(\text{Hg}-\text{O}) + \nu(\text{Te}-\text{O})]$ -type occur in a frequency range similar to that of $\text{Hg}(\text{OTeF}_5)_2$. As observed for the “asymmetric” $[\nu(\text{Hg}-\text{O}) - \nu(\text{Te}-\text{O})]$ -type modes, the “symmetric” modes occur at higher frequencies for the XeF_2 complex (exptl, $474/478$ and 508 cm^{-1}) than those of the KrF_2 complex (exptl, 458 and 484 cm^{-1}). In the case of the XeF_2 complex, a third band occurs at 445 cm^{-1} which has an additional coupling with $\nu(\text{Xe}_{16}-\text{F}_{23})$ in the theoretical model. In the KrF_2 complex, only two $[\nu(\text{Hg}-\text{O}) + \nu(\text{Te}-\text{O})]$ -type modes are predicted where $[\nu(\text{Hg}_{12}-\text{O}_{28}) + \nu(\text{Te}_{14}-\text{O}_{28})]$ is only coupled in-phase (exptl, 458 cm^{-1} ; calcd, 505 cm^{-1}) or out-of-phase (exptl, 484 cm^{-1} ; calcd, 527 cm^{-1}) with $[\nu(\text{Hg}_{12}-\text{O}_{31}) + \nu(\text{Te}_{15}-\text{O}_{31})]$. In the XeF_2 complex, only one mode is predicted in which $[\nu(\text{Hg}_{12}-\text{O}_{28}) + \nu(\text{Te}_{14}-\text{O}_{28})]$ is out-of-phase coupled with $[\nu(\text{Hg}_{12}-\text{O}_{31}) + \nu(\text{Te}_{15}-\text{O}_{31})]$ (exptl, 508 cm^{-1} ; calcd, 524 cm^{-1}). Two modes are predicted where $[\nu(\text{Hg}_{12}-\text{O}_{28}) + \nu(\text{Te}_{14}-\text{O}_{28})]$ is in-phase coupled with $[\nu(\text{Hg}_{12}-\text{O}_{31}) + \nu(\text{Te}_{15}-\text{O}_{31})]$ (exptl, $478/474$ and 445 cm^{-1} ; calcd, 502 and 499 cm^{-1}) because, in both cases, there is additional coupling with $\nu(\text{Xe}_{16}-\text{F}_{23})$ and/or analogous modes of the terminal $\text{Hg}(\text{OTeF}_5)_2$ units.

The calculated vibrational displacements show that the stretching modes of the bridging KrF_2 and XeF_2 units are extensively coupled and reveal differences between their inter- and intraligand couplings in their respective complexes. The four coupled modes of the KrF_2 complex are each comprised of inter- and intraligand coupling components, whereas there is less intraligand coupling in the XeF_2 complex. Instead, some coupling with the terminal $\text{Hg}(\text{OTeF}_5)_2$ units occurs. Coupling among the stretching modes of the NgF_2 units in the $[\text{BrOF}_2][\text{AsF}_6] \cdot 2\text{XeF}_2$ ⁴ and $[\text{BrOF}_2][\text{AsF}_6] \cdot 2\text{KrF}_2$ ¹⁵ complexes has also been observed.

The modes derived from the symmetric (Raman-active and infrared-inactive) stretches of the free NgF_2 molecules, i.e., $[\nu(\text{Ng}_{13}-\text{F}_{17}) + \nu(\text{Ng}_{13}-\text{F}_{20})]$ and $[\nu(\text{Ng}_{16}-\text{F}_{23}) + \nu(\text{Ng}_{16}-\text{F}_{40})]$, are expected to occur at lower frequency than those derived from the asymmetric stretching mode of free NgF_2 , i.e., $[\nu(\text{Ng}_{13}-\text{F}_{17}) - \nu(\text{Ng}_{13}-\text{F}_{20})]$ and $[\nu(\text{Ng}_{16}-\text{F}_{23}) - \nu(\text{Ng}_{16}-\text{F}_{40})]$. The “symmetric” modes in the KrF_2 complex are expected to in-phase couple, $[\nu(\text{Kr}_{13}-\text{F}_{17}) + \nu(\text{Kr}_{13}-\text{F}_{20})] + [\nu(\text{Kr}_{16}-\text{F}_{23}) + \nu(\text{Kr}_{16}-\text{F}_{40})]$, and out-of-phase couple, $[\nu(\text{Kr}_{13}-\text{F}_{17}) + \nu(\text{Kr}_{13}-\text{F}_{20})] - [\nu(\text{Kr}_{16}-\text{F}_{23}) + \nu(\text{Kr}_{16}-\text{F}_{40})]$. The latter modes were calculated at 512 and 513 cm^{-1} and are assigned to a single band at 468 cm^{-1} , the most intense band in the Raman spectrum. In the XeF_2 complex, the totally in-phase analogue, $[\nu(\text{Xe}_{13}-\text{F}_{17}) + \nu(\text{Xe}_{13}-\text{F}_{20})] + [\nu(\text{Xe}_{16}-\text{F}_{23}) + \nu(\text{Xe}_{16}-\text{F}_{40})]$, is observed at 501 cm^{-1} and is also a strong band. In addition, there are two bands corresponding to the out-of-phase stretching mode, $[\nu(\text{Xe}_{13}-\text{F}_{17})] - [\nu(\text{Xe}_{16}-\text{F}_{23})]$ (489 cm^{-1}) and $[\nu(\text{Xe}_{13}-\text{F}_{20})] - [\nu(\text{Xe}_{16}-\text{F}_{40})]$ (508

cm^{-1}). These frequencies are comparable to the Raman-active $\nu_s(\text{Ng}-\text{F}_2)$ mode of free NgF_2 (Xe, 494 cm^{-1} ;³⁷ Kr, 464 cm^{-1})³⁸ and are in accordance with the observed Ng–F bond lengths (Xe, $1.981(4)$ – $2.012(4)$ Å and Kr, $1.883(3)$ – $1.897(3)$ Å in the complexes; Xe, $1.999(4)$ Å³ and Kr, $1.894(5)$ Å² in free NgF_2). The corresponding calculated NgF_2 frequencies and Ng–F bond lengths of the complexes and free NgF_2 follow the same trend (Xe: $516, 521, 510 \text{ cm}^{-1}$, 1.991 – 2.003 Å and Kr: $513, 512 \text{ cm}^{-1}$, 1.868 – 1.878 Å; free XeF_2 : 530 cm^{-1} , 1.980 Å and free KrF_2 : 519 cm^{-1} , 1.865 Å). In both complexes, the “symmetric” stretching mode appears at slightly higher frequency than the symmetric stretching mode of free NgF_2 . The “symmetric” stretch of the XeF_2 complex appears at lower frequency than other “symmetric” stretching modes of the bridging XeF_2 molecules in the Cd^{2+} coordination complexes, $\text{Cd}(\text{XeF}_2)_4(\text{AsF}_6)_2$ (521 cm^{-1})¹⁰ and $\text{Cd}(\text{XeF}_2)_5(\text{PF}_6)_2$ (521 cm^{-1}).¹¹

The bands at 558 and 553 (Kr) cm^{-1} and 518 (Xe) cm^{-1} are assigned to NgF_2 stretching modes that are derived from the asymmetric (infrared-active and Raman-inactive) stretches of the free NgF_2 molecules. In order to understand why the formally Raman inactive bands in free NgF_2 are observed in the Raman spectra of both NgF_2 complexes, the positioning of the two crystallographically inequivalent NgF_2 molecules in the crystal structures must be taken into account. One NgF_2 molecule is positioned on an inversion center, so that the vibrational activities of the corresponding stretching modes will be the same as those of free NgF_2 , i.e., the symmetric stretch will be Raman active and the asymmetric stretch will be infrared active. The second NgF_2 molecule is on a general position, resulting in two crystallographically inequivalent Ng–F bonds. As a result, both coupled modes derived from the asymmetric stretch of free NgF_2 will be Raman and infrared active. The $[\text{Hg}(\text{OTeF}_5)_2]_3 \cdot 2\text{NgF}_2$ models (C_1 symmetry) display this behavior.

The “asymmetric” NgF_2 stretches are coupled in-phase, $[\nu(\text{Ng}_{13}-\text{F}_{17}) - \nu(\text{Ng}_{13}-\text{F}_{20})] + [\nu(\text{Ng}_{16}-\text{F}_{23}) - \nu(\text{Ng}_{16}-\text{F}_{40})]$ (Xe, 518 cm^{-1} ; Kr, 558 cm^{-1}), and out-of-phase, $[\nu(\text{Ng}_{13}-\text{F}_{17}) - \nu(\text{Ng}_{13}-\text{F}_{20})] - [\nu(\text{Ng}_{16}-\text{F}_{23}) - \nu(\text{Ng}_{16}-\text{F}_{40})]$ (Xe, 518 cm^{-1} ; Kr, 553 cm^{-1}). These “asymmetric” modes occur at lower frequencies than their infrared-active asymmetric counterparts in free XeF_2 (555 cm^{-1})³⁷ and KrF_2 (580 cm^{-1}).³⁹ This trend is reproduced by the calculations (Xe, $521/524$ and $528/534 \text{ cm}^{-1}$; Kr, 574 and 560 cm^{-1} for NgF_2 in the complexes; Xe, 568 cm^{-1} ; Kr, 607 cm^{-1} in free NgF_2). It is noteworthy that, although the XeF_2 bridging molecules in $\text{Cd}(\text{XeF}_2)_4(\text{AsF}_6)_2$,¹⁰ $\text{Cd}(\text{XeF}_2)_5(\text{PF}_6)_2$,¹¹ $\text{Ca}(\text{XeF}_2)_n(\text{AsF}_6)_2$ ($n = 4, 2.5$),⁴⁰ $\text{Ca}_2(\text{XeF}_2)_9(\text{AsF}_6)_4$,⁴¹ $\text{Ca}(\text{XeF}_2)_5(\text{PF}_6)_2$,¹¹ $\text{Sr}_3(\text{XeF}_2)_{10}(\text{PF}_6)_6$,⁸ and $\text{Pb}_3(\text{XeF}_2)_{11}(\text{PF}_6)_6$,⁸ also have two crystallographically inequivalent Xe–F bonds, their “asymmetric” XeF_2 stretches were not identified.

As previously observed for $[\text{BrOF}_2][\text{AsF}_6] \cdot 2\text{NgF}_2$,^{4,15} the double degeneracy of the NgF_2 bending modes of free NgF_2 (ν_2, Π_u) is removed when NgF_2 is asymmetrically fluorine bridged to mercury, resulting in splitting into out-of-plane, $\delta(\text{NgF}_2)_{\text{o.o.p.}}$, and in-plane, $\delta(\text{NgF}_2)_{\text{i.p.}}$, modes with respect to the plane containing both NgF_2 ligands. The bending modes are observed at 223 and 241 cm^{-1} (Xe) and at 237 and 260 cm^{-1} (Kr) and are slightly shifted to higher frequencies relative to those of free XeF_2 (213 cm^{-1})³⁷ and free KrF_2 (236 cm^{-1}).³⁹ The calculated and experimental frequencies are also in good agreement (Xe: $218, 219, 221$, and 236 cm^{-1} ; Kr: $252, 252,$

254 , and 266 cm^{-1} for NgF_2 in the complexes; cf., Xe, 215 cm^{-1} ; Kr, 250 cm^{-1} in free NgF_2).

COMPUTATIONAL RESULTS

Unless otherwise noted, the following discussion refers to the central units of the gas-phase model compounds, $[\text{Hg}(\text{OTeF}_5)_2]_3$ and $[\text{Hg}(\text{OTeF}_5)_2]_3 \cdot 2\text{NgF}_2$.

Calculated Geometries. *Hg(OTeF₅)₂ and [Hg(OTeF₅)₂]₃.* The gas-phase geometry of monomeric $\text{Hg}(\text{OTeF}_5)_2$ (C_2) (Figure 6a) was optimized at the B3LYP and PBE1PBE levels of theory using the def2-TZPP and aug-cc-PTVZ basis sets, resulting in stationary points with all frequencies real (Table S1). The calculated bond lengths and angles are provided in Table S7. Although both levels of theory well reproduced the observed trends (see Raman Spectroscopy), better agreement was obtained at the PBE1PBE level. All attempts to optimize the monomeric $\text{Hg}(\text{OTeF}_5)_2$ unit, regardless of the starting geometry, resulted in an *anti*-conformation (C_2 symmetry) resembling that observed (C_{2h} in the crystal structure) and calculated (C_2) for $\text{Xe}(\text{OTeF}_5)_2$.³² The authors were unable to reproduce the previously reported³⁰ calculated C_{2h} geometry for $\text{Hg}(\text{OTeF}_5)_2$. However, the *anti*-conformation of the gas-phase $\text{Hg}(\text{OTeF}_5)_2$ monomer contrasts with the *gauche*-conformation observed in the crystal structure. The optimization of the presently unknown trimer, $[\text{Hg}(\text{OTeF}_5)_2]_3$ (Figures 6b and S5), using the PBE1PBE/def2-TZPP method also resulted in a stationary point with all frequencies real (C_1 symmetry). This model reproduced the observed *gauche*-conformation of the central $\text{Hg}(\text{OTeF}_5)_2$ molecule showing that crystal packing and accompanying Hg---O contacts (2.737 Å) with neighboring terminal $\text{Hg}(\text{OTeF}_5)_2$ molecules are likely major factors in stabilizing the solid-state *gauche*-conformation. This is supported by the fact that the two terminal $\text{Hg}(\text{OTeF}_5)_2$ units also retain the *gauche*-conformation with similar Hg---O contacts (2.775 Å). Because of its size, the unknown trimer was only calculated with the smaller basis set, def2-TZPP.

In the trimer, the largest discrepancies occur for the Hg---O(1A,1C) secondary bonding interactions (calcd, 2.737 Å; exptl, $2.641(7)$ Å) and the O(1)–Hg---O(1A,1C) bond angles (calcd, 73.0 and 103.8° ; exptl, 78.7 and $93.8(3)^\circ$). These differences are likely attributable to the model itself, where the Hg---F secondary contacts are absent for the central $\text{Hg}(\text{OTeF}_5)_2$ unit. Ideally, a total of five $\text{Hg}(\text{OTeF}_5)_2$ molecules would be required to reproduce all secondary contacts observed in the crystal structure. The calculated O–Hg–O bond angle (176.0°) is more open than the observed angle in $\text{Hg}(\text{OTeF}_5)_2$ ($170.5(4)^\circ$) (see X-ray Crystallography), but is in close agreement with the O–Hg–O angle calculated for $\text{Hg}(\text{OTeF}_5)_2$ monomer (calcd, 176.8°).

The Hg–O bond lengths of the calculated gas-phase $[\text{Hg}(\text{OTeF}_5)_2]_3$ molecule (2.008 Å) are in better agreement with the experimental bond length ($2.016(6)$ Å) than the calculated Hg–O bond lengths of $\text{Hg}(\text{OTeF}_5)_2$ (1.976 Å). The Te–F and Te–O bond lengths are overall slightly shorter for the calculated structure of $[\text{Hg}(\text{OTeF}_5)_2]_3$ (1.832 – 1.855 and 1.865 Å, respectively) when compared with those calculated for monomeric $\text{Hg}(\text{OTeF}_5)_2$ (1.835 – 1.866 and 1.856 Å, respectively), but are also in better agreement with those observed for solid $\text{Hg}(\text{OTeF}_5)_2$ (Table 2).

[Hg(OTeF₅)₂]₃ · 2NgF₂ (Ng = Xe, Kr). The calculated gas-phase geometries of the model complexes, $[\text{Hg}(\text{OTeF}_5)_2]_3 \cdot 2\text{NgF}_2$

(Ng = Xe, Kr) (Figures 7 and S6, Table 7), were optimized at the PBE1PBE level of theory using the def2-TZVP basis set,

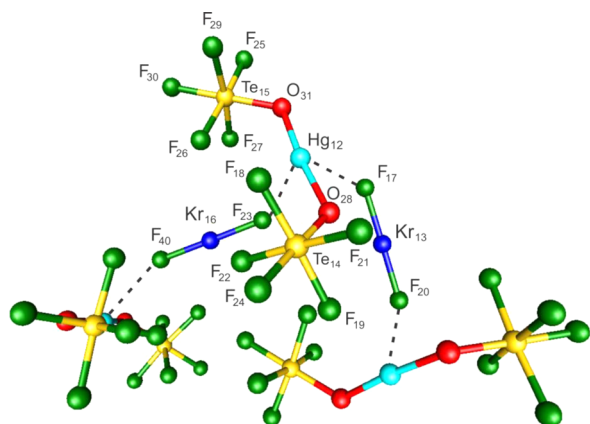


Figure 7. The gas-phase, energy-minimized geometry of $[\text{Hg}(\text{OTeF}_5)_2]_3 \cdot 1.5\text{KrF}_2$ calculated at the PBE1PBE/def2-TZVP level of theory. The dashed lines show the contacts between the Hg(II) atom of the central $\text{Hg}(\text{OTeF}_5)_2$ unit and two fluorine atoms of two adjacent KrF_2 molecules.

resulting in stationary points with all frequencies real (Tables S3 and S4). These systems were too large and demanding of CPU time to be optimized using the larger aug-cc-PTVZ basis set. The calculated structures of $[\text{Hg}(\text{OTeF}_5)_2]_3 \cdot 2\text{NgF}_2$ mimic the local environments of both $\text{Hg}(\text{OTeF}_5)_2$ and NgF_2 in the crystal structures of $\text{Hg}(\text{OTeF}_5)_2 \cdot 1.5\text{NgF}_2$. The central $\text{Hg}(\text{OTeF}_5)_2$ unit of the starting models takes into account the two shorter Hg---F(NgF) contacts that are *trans* to one another. In the optimized geometries, the central $\text{Hg}(\text{OTeF}_5)_2$ units retained the *gauche*-conformation observed in the crystal structures, as was calculated for the central $\text{Hg}(\text{OTeF}_5)_2$ unit of $[\text{Hg}(\text{OTeF}_5)_2]_3$. The calculated models retained the two Hg---F(NgF) contacts to the central Hg atom (Xe, 2.724 and 2.723 Å; Kr, 2.762 and 2.754 Å) but optimized so that the Hg---F(NgF) secondary bonds are *cis* to one another with contact distances that better reproduce the longer Hg---F(NgF) contacts observed in the crystal structures (Xe, 2.701(5) Å; Kr, 2.741(3) Å). In both the Kr and Xe models, one of the outer $\text{Hg}(\text{OTeF}_5)_2$ units optimized to a *syn*-conformation (Te—O—Hg—O—Te dihedral angles of 126.5° for Xe and 122.8° for Kr), when only a single, long secondary Hg---F(NgF) bond is present (Xe, 2.746 Å; Kr, 2.816 Å). In contrast, the other terminal $\text{Hg}(\text{OTeF}_5)_2$ unit optimized to a *gauche*-conformation presumably because the secondary Hg---F(NgF) contacts (Xe, 2.694 Å; Kr, 2.739 Å) are somewhat shorter and more covalent. These differences are reminiscent of those observed for the $[\text{Hg}(\text{OTeF}_5)_2]_3$ model (vide supra) and may also result from the model's inability to take into account two additional Hg---F and Hg---O secondary contacts that are also present in the crystal structures (see X-ray Crystallography).

The complexed NgF_2 molecules are essentially linear with F—Ng—F angles (Xe, 179.2 and 179.1°; Kr, 179.5 and 179.3°) and Ng—F bond lengths (Xe, 1.991–2.003 Å; Kr, 1.868–1.878 Å) that well reproduce those observed in the crystal structures (Xe: 180 and 179.4(2)°, 1.981(4)–2.012(4) Å; Kr: 180 and 178.9(1)°, 1.883(3)–1.897(3) Å). The calculated Ng—F bond lengths are slightly underestimated for free NgF_2 (calcd: Xe, 1.980 Å and Kr, 1.865 Å; exptl: Xe, 1.999(4) Å³ and Kr, 1.894(5) Å²).

Table 7. Calculated Geometrical Parameters^a for $\text{Hg}(\text{OTeF}_5)_2 \cdot 1.5\text{NgF}_2$ (Ng = Xe, Kr)

	Xe	Kr	Xe	Kr
Bond Lengths (Å)				
Hg ₁₂ —O ₃₁	1.991	1.988	Te ₁₄ —F ₁₈	1.854
Hg ₁₂ —O ₂₈	2.002	2.000	Te ₁₄ —F ₂₄	1.834
O ₃₁ —Te ₁₅	1.847	1.849	Te ₁₄ —F ₂₂	1.854
O ₂₈ —Te ₁₄	1.847	1.849	Te ₁₄ —F ₂₁	1.839
Te ₁₅ —F ₂₇	1.852	1.851	Hg ₁₂ ---F ₂₃	2.723
Te ₁₅ —F ₂₉	1.843	1.843	Hg ₁₂ ---F ₁₇	2.724
Te ₁₅ —F ₂₆	1.870	1.869	Ng ₁₆ —F ₂₃	2.003
Te ₁₅ —F ₂₅	1.836	1.835	Ng ₁₆ —F ₄₀	1.991
Te ₁₅ —F ₃₀	1.838	1.838	Ng ₁₃ —F ₁₇	1.997
Te ₁₄ —F ₁₉	1.855	1.855	Ng ₁₃ —F ₂₀	1.993
Bond Angles (°)				
O ₃₁ —Hg ₁₂ —O ₂₈	173.6	173.7	F ₂₆ —Te ₁₅ —F ₂₅	176.4
Hg ₁₂ —O ₃₁ —Te ₁₅	122.4	122.4	F ₂₇ —Te ₁₅ —F ₂₉	173.8
Hg ₁₂ —O ₂₈ —Te ₁₄	123.6	122.4	F ₂₄ —Te ₁₄ —F ₂₂	87.3
O ₃₁ —Te ₁₅ —F ₂₇	93.1	93.0	F ₂₄ —Te ₁₄ —F ₁₉	88.0
O ₃₁ —Te ₁₅ —F ₂₉	92.9	92.8	F ₂₄ —Te ₁₄ —F ₁₈	88.6
O ₃₁ —Te ₁₅ —F ₂₆	92.5	92.5	F ₂₄ —Te ₁₄ —F ₂₁	87.7
O ₃₁ —Te ₁₅ —F ₂₅	91.0	90.9	F ₂₂ —Te ₁₄ —F ₁₈	89.2
O ₃₁ —Te ₁₅ —F ₃₀	179.8	179.8	F ₁₈ —Te ₁₄ —F ₂₁	90.8
O ₂₈ —Te ₁₄ —F ₁₉	90.3	90.4	F ₂₁ —Te ₁₄ —F ₁₉	89.8
O ₂₈ —Te ₁₄ —F ₁₈	93.0	92.9	F ₁₉ —Te ₁₄ —F ₂₂	90.0
O ₂₈ —Te ₁₄ —F ₂₄	178.3	178.4	F ₂₂ —Te ₁₄ —F ₂₁	175.0
O ₂₈ —Te ₁₄ —F ₂₂	92.9	92.7	F ₁₉ —Te ₁₄ —F ₁₈	176.6
O ₂₈ —Te ₁₄ —F ₂₁	92.1	92.1	F ₄₀ —Ng ₁₆ —F ₂₃	179.2
F ₃₀ —Te ₁₅ —F ₂₉	87.3	87.3	F ₁₇ —Ng ₁₃ —F ₂₀	179.1
F ₃₀ —Te ₁₅ —F ₂₆	87.6	87.7	Ng ₁₆ —F ₂₃ ---Hg ₁₂	138.4
F ₃₀ —Te ₁₅ —F ₂₅	88.9	88.9	Ng ₁₃ —F ₁₇ ---Hg ₁₂	118.3
F ₃₀ —Te ₁₅ —F ₂₇	86.8	86.9	O ₃₁ —Hg ₁₂ ---F ₂₃	97.3
F ₂₉ —Te ₁₅ —F ₂₅	91.0	91.0	O ₃₁ —Hg ₁₂ ---F ₁₇	99.7
F ₂₅ —Te ₁₅ —F ₂₇	90.7	90.7	O ₂₈ —Hg ₁₂ ---F ₂₃	87.1
F ₂₇ —Te ₁₅ —F ₂₆	88.3	88.3	O ₂₈ —Hg ₁₂ ---F ₁₇	76.8
F ₂₆ —Te ₁₅ —F ₂₉	89.6	89.6	F ₁₇ ---Hg ₁₂ ---F ₂₃	75.8
Dihedral Angle (°)				
Te ₁₅ —O ₃₁ —Hg ₁₂ —O ₂₈ — Te ₁₄				31.0
				34.0

^aThe atom labeling scheme corresponds to that used in Figures 7 and S6 for Xe and Kr, respectively. All bond lengths and angles refer to the central $\text{Hg}(\text{OTeF}_5)_2$ unit and to the coordinated NgF_2 molecules of the unknown $[\text{Hg}(\text{OTeF}_5)_2]_3 \cdot 2\text{NgF}_2$ molecules calculated at the PBE1PBE/def2-TZVP level of theory.

The Hg—O (Xe: 1.991, 2.002 Å; Kr: 1.998, 2.000 Å) and Te—O (Xe: 1.847 Å; Kr: 1.849 Å) bond lengths are slightly under- and overestimated, respectively, compared to the Hg—O (Xe: 2.015(5), 2.037(5) Å; Kr: 2.017(3), 2.029(3) Å) and Te—O (Xe: 1.815(5), 1.811(6) Å; Kr: 1.819(3), 1.836(3) Å) bond lengths in the crystal structures of $\text{Hg}(\text{OTeF}_5)_2 \cdot 1.5\text{NgF}_2$. The calculated O—Hg—O bond angles (Xe, 173.6°; Kr, 173.7°) accurately reproduce the observed O—Hg—O bond angles (Xe, 173.0(2)°; Kr, 173.3(1)°) of the complexes, whereas the Hg—O—Te bond angles (Xe: 122.4, 123.6°; Kr: 122.4°) are smaller than observed (Xe: 132.8(3), 127.2(3)°; Kr: 129.6(2), 126.5(1)°). This may reflect the elongation of the secondary bonding interactions and the absence of the two additional Hg---F and Hg---O contacts that are present in the crystal structure. This limitation in the model may contribute to the calculated Te—O—Hg—O—Te dihedral angles (Xe, 31.0°; Kr, 34.0°) which give a central $\text{Hg}(\text{OTeF}_5)_2$ unit that more closely approximates a *syn*-conformation than those observed in the

solid state (Xe, 45.2(5)°; Kr, 50.3(3)°). All Te–F bond lengths (Xe, 1.834–1.870 Å; Kr, 1.833–1.869 Å) are in the same ranges as those observed in the crystal structures (Xe, 1.814(5)–1.845(4) Å; Kr, 1.824(3)–1.848(3) Å) with the exception of the Te₁₅–F₂₆ bond lengths (Xe, 1.870 Å; Kr, 1.869 Å), which are slightly longer.

Natural Bond Orbital (NBO) Analyses. The NBO analyses reported in this section (Table S8) refer to the central Hg(OTeF₅)₂ units of [Hg(OTeF₅)₂]₃ and [Hg(OTeF₅)₂]₃·2NgF₂ (Figures 6, 7, and S6) unless noted otherwise.

When compared with gas-phase Hg(OTeF₅)₂, the charge on Hg is little affected by contacts with adjacent units within [Hg(OTeF₅)₂]₃. The situation is essentially the same when NgF₂ coordinates to [Hg(OTeF₅)₂]₃, providing the model complexes, [Hg(OTeF₅)₂]₃·2NgF₂. The highest negative charges reside on the O atoms of [Hg(OTeF₅)₂]₃ (–1.208), with their charges becoming more positive upon NgF₂ coordination (Kr and Xe, –1.137). This is reflected by small increases in the Hg–O bond orders from 0.320 to 0.419/0.439 for KrF₂ and to 0.413/0.434 for XeF₂ and in the oxygen atom valencies from 0.948 to 1.025/1.015 for KrF₂ and to 1.023/1.011 for XeF₂. Little change in the Te–O bond orders and Te valencies occurs upon NgF₂ coordination.

In each NgF₂ complex, there are small negative charge transfers from both NgF₂ ligands (Kr, 0.033/0.045; Xe, 0.040/0.052) to the central Hg(OTeF₅)₂ units (Kr, –0.038; Xe, –0.046) and combined charge transfers to the two terminal Hg(OTeF₅)₂ units (Kr, –0.040; Xe, –0.046). The small Hg–F(Ng) bridge bond orders (~0.06) and small degrees of NgF₂ polarization by the central Hg(OTeF₅)₂ unit of [Hg(OTeF₅)₂]₃ are consistent with weak covalent interactions between the Hg(II) acceptor sites and the σ-donor fluorine ligands of NgF₂.

CONCLUSION

The –OTeF₅ analogue of HgF₂, Hg(OTeF₅)₂, was structurally characterized by single-crystal X-ray diffraction and the low-temperature Raman spectrum was assigned using quantum-chemical calculations. The crystal structure of Hg(OTeF₅)₂ showed that the Hg(OTeF₅)₂ molecules are not isolated but participate in a chain structure that results from long Hg–O and Hg–F secondary bonding interactions with Hg(II) centers of adjacent Hg(OTeF₅)₂ molecules. The Raman spectrum was assigned using the calculated vibrational frequencies and intensities of the hypothetical trimer, [Hg(OTeF₅)₂]₃, which reproduced the solid-state *gauche*-conformation and the shortest Hg–O contacts observed in the crystal structure. The *gauche*-conformation was rationalized based on the occurrence of secondary Hg–F and Hg–O bonding interactions with the Hg(II) center. In contrast, the optimized gas-phase structure of monomeric Hg(OTeF₅)₂ provided a geometry having its –OTeF₅ groups in an *anti*-conformation similar to that observed in Xe(OTeF₅)₂. The coordination complexes, Hg(OTeF₅)₂·1.5NgF₂ (Ng = Xe, Kr), were also synthesized and structurally characterized by single-crystal X-ray diffraction and low-temperature Raman spectroscopy. In both chain structures, the NgF₂ molecules form bridges between mercury centers by coordination to the metal through their fluorine ligands. The contact distances between Hg(II) and the F atoms of XeF₂ are shorter than those of the KrF₂ analogue, consistent with the greater ionic character of the Xe–F bonds in XeF₂. NBO analyses are consistent with weak covalent interactions between the Hg(OTeF₅)₂ acceptor and the NgF₂ σ-donor ligands. The calculated frequencies and

intensities of [Hg(OTeF₅)₂]₃·2NgF₂ aided in the assignment of the experimental Raman spectra of Hg(OTeF₅)₂·1.5NgF₂. The Hg(OTeF₅)₂·1.5NgF₂ complexes are currently the only examples of coordination complexes in which KrF₂ and XeF₂ are coordinated to mercury in a neutral compound and provide the only example of a bridging KrF₂ ligand.

EXPERIMENTAL SECTION

Caution. Anhydrous HF must be handled using appropriate protective gear with immediate access to proper treatment procedures^{42–44} in the event of contact with liquid HF, HF vapor, or HF-containing solutions. Krypton difluoride and its coordination complex, Hg(OTeF₅)₂·1.5KrF₂, are highly energetic materials and strong oxidizers that are only stable under the rigorously anhydrous handling conditions employed in the experimental procedures outlined below. Both compounds are likely to detonate upon contact with organic materials. Thus, adequate protective apparel and working behind adequate shielding are crucial for the safe manipulation of these materials. It is therefore recommended that the syntheses of the aforementioned compounds be carried out on small scales (<200 mg).

Apparatus and Materials. *General.* Manipulations involving air-sensitive materials were carried out under anhydrous conditions on glass and metal high-vacuum lines and inside an inert atmosphere drybox as previously described.⁴⁵ Preparative work was carried out in reaction vessels constructed from 1/4-in. o.d. (1/16-in. wall thickness) lengths of FEP (tetrafluoroethylene-hexafluoropropylene block copolymer) tubing. The tubing was heat-sealed at one end, heat flared at the other end, and connected through a 45° SAE flare nut to the conical end of a Kel-F (chlorotrifluoroethylene polymer) valve to form a compression seal. Reaction vessels and sample tubes were rigorously dried under dynamic vacuum prior to passivation for at least 8 h with 1 atm of F₂ gas. Vacuum line connections were made using 1/4-in. 316 stainless steel Swagelok Ultratorr unions fitted with Viton O-rings.

Xenon difluoride⁴⁶ and KrF₂^{2,47,48} were prepared and purified as previously described. High-purity HgF₂ and HOTeF₅ were prepared using synthetic procedures outlined in the Supporting Information. Anhydrous HF (Harshaw Chemicals Co.) was purified as previously described.⁴⁹ Methylene chloride (Caledon, reagent grade) was dried over previously vacuum-dried (250 °C) Davison type 3 Å molecular sieves (Fisher Scientific) for 3 days followed by vacuum distillation into a dry glass bulb equipped with a 4-mm J. Young (glass/Teflon) valve. Methylene chloride-*d*₂ (D, 99.5%; BDH Chemicals) was dried over CaH₂ powder (99.5%, BDH Chemicals). Sulfuryl chloride fluoride (Allied Chemical, Baker Adamson Division) was purified as previously described.⁵⁰ High-purity Ar (99.998%, Air Liquide) or N₂ (obtained from liquid N₂ boil-off and dried by passage through a column of dry 3 Å molecular sieves) gases were used for backfilling reaction and sample vessels.

Synthesis of Hg(OTeF₅)₂ and Crystal Growth. A passivated FEP reaction vessel equipped with a Kel-F valve was loaded with HgF₂ (0.4938 g, 2.069 mmol) inside a drybox. The reaction vessel was then transferred to a metal vacuum line where HOTeF₅ was distilled into it. The contents of the reaction vessel were allowed to react at 50 °C for several hours with periodic agitation. Residual HOTeF₅, observed by Raman spectroscopy, and HF formed in the reaction (eq 1) were removed by pumping under dynamic vacuum for 3 h at room temperature, resulting in a friable, white solid in essentially quantitative yield (99.1%). The Raman spectrum of the product was recorded at –150 °C (Figure S1).

Crystals of Hg(OTeF₅)₂ were grown by slow evaporation of a CH₂Cl₂ solution. The solution was prepared in a 1/4-in. o.d. FEP T-shaped reaction vessel by dissolving Hg(OTeF₅)₂ (0.0314 g, 0.0463 mmol) in ~0.3 mL of CH₂Cl₂ at room temperature under anhydrous conditions. The void above the solution was backfilled with 0.5 atm of dry N₂ at –78 °C. A temperature gradient was established by cooling the empty side arm of the vessel to –78 °C in a dry ice/acetone bath while maintaining the solution at 0 °C. This temperature gradient resulted in slow evaporation of the CH₂Cl₂ solvent and growth of colorless crystals over the course of 11 days. The side arm containing

the evaporated supernatant was then cooled to $-196\text{ }^{\circ}\text{C}$ and heat-sealed off under dynamic vacuum. The crystalline material was further dried at $-78\text{ }^{\circ}\text{C}$ under dynamic vacuum. A $\text{Hg}(\text{OTeF}_5)_2$ crystal having the dimensions of $0.22 \times 0.10 \times 0.04\text{ mm}^3$ was selected for a low-temperature X-ray structure determination.

In the sections that follow, square brackets denote quantities/conditions used for crystal growth and unbracketed quantities/conditions denote Raman sample preparations.

Synthesis of $\text{Hg}(\text{OTeF}_5)_2 \cdot 1.5\text{XeF}_2$ and Crystal Growth. In a typical synthesis, 0.1816 g (0.2679 mmol) [0.0879 g (0.1298 mmol)] of $\text{Hg}(\text{OTeF}_5)_2$ was weighed, inside a drybox, into a $1/4$ -in. o.d. quartz [T-shaped FEP] reaction vessel equipped with a 4-mm J. Young [Kel-F] valve. Xenon difluoride, 0.0750 g (0.443 mmol) [0.0267 g (0.1578 mmol)], was added to the reactor at $-140\text{ }^{\circ}\text{C}$ inside the drybox. The reactor was removed from the drybox at $-196\text{ }^{\circ}\text{C}$ and attached to a glass vacuum line while maintaining the reagents at $-78\text{ }^{\circ}\text{C}$. Sulfuryl chloride fluoride ($\sim 0.2\text{ mL}$) was condensed onto the reagents, and the temperature was increased to $0\text{ }^{\circ}\text{C}$ for 5 min and continuously agitated to dissolve the reactants. The solvent was removed from the Raman sample under dynamic vacuum at $-78\text{ }^{\circ}\text{C}$ leaving behind a white solid. The Raman spectrum of the product was recorded at $-155\text{ }^{\circ}\text{C}$. The solution used for crystallization was pale yellow and was cooled to $-78\text{ }^{\circ}\text{C}$. Over the course of 5 days, colorless crystals formed. The supernatant was decanted into the side arm of the T-shaped FEP vessel at $-78\text{ }^{\circ}\text{C}$. Once the majority of the supernatant had been transferred, the contents of the side arm were cooled to $-196\text{ }^{\circ}\text{C}$, and the supernatant was isolated and removed by heat sealing off this portion of the reaction vessel under dynamic vacuum at $-196\text{ }^{\circ}\text{C}$. This was followed by removal of the residual solvent from the crystalline sample under dynamic vacuum at $-78\text{ }^{\circ}\text{C}$. A $\text{Hg}(\text{OTeF}_5)_2 \cdot 1.5\text{XeF}_2$ crystal having the dimensions $0.25 \times 0.04 \times 0.04\text{ mm}^3$ was selected for a low-temperature X-ray structure determination.

Synthesis of $\text{Hg}(\text{OTeF}_5)_2 \cdot 1.5\text{KrF}_2$ and Crystal Growth. In a typical synthesis, KrF_2 was sublimed under static vacuum from a FEP storage container at room temperature into a preweighed, fluorine-passivated 4-mm o.d. FEP vessel cooled to $-196\text{ }^{\circ}\text{C}$. Krypton difluoride, 0.0161 g (0.132 mmol) [0.0538 g (0.4417 mmol)], was condensed under static vacuum through a FEP connection into a fluorine-passivated $1/4$ -in. o.d. quartz [T-shaped FEP] reaction vessel cooled to $-196\text{ }^{\circ}\text{C}$ that had been previously loaded with $\text{Hg}(\text{OTeF}_5)_2$, 0.0404 g (0.0596 mmol) [0.1152 g (0.1610 mmol)] inside a drybox. Sulfuryl chloride fluoride was condensed onto the reagents ($\sim 0.3\text{ mL}$) [$\sim 0.5\text{ mL}$], and upon warming the reaction vessel to $-20\text{ }^{\circ}\text{C}$ for 2 min, the solid mixture partially dissolved to give a pale yellow solution plus a suspension of white solid. The reaction mixture used for preparation of the Raman sample was allowed to react at $-78\text{ }^{\circ}\text{C}$ for 3 h followed by removal of SO_2ClF under dynamic vacuum at $-78\text{ }^{\circ}\text{C}$. The Raman spectrum of the product was recorded at $-155\text{ }^{\circ}\text{C}$. The FEP reaction vessel and solution used for crystal growth were maintained at $-78\text{ }^{\circ}\text{C}$ for 2 weeks. Crystals were isolated as described in the section above. A $\text{Hg}(\text{OTeF}_5)_2 \cdot 1.5\text{KrF}_2$ crystal having the dimensions $0.18 \times 0.08 \times 0.05\text{ mm}^3$ was selected for a low-temperature X-ray structure determination.

X-ray Crystallography. Crystal Mounting Procedure. All crystalline products were stored at $-78\text{ }^{\circ}\text{C}$ until a suitable crystal could be selected and mounted on the X-ray diffractometer using a previously described low-temperature crystal mounting technique.⁵¹ Dried crystalline samples that had been maintained at $-78\text{ }^{\circ}\text{C}$ were dumped, without warming, into an aluminum trough cooled to $-110 \pm 5\text{ }^{\circ}\text{C}$ by means of a cold stream of dry N_2 gas, allowing selection of individual crystals under a stereomicroscope. Single crystals were mounted at the tip of a glass fiber at $-110 \pm 5\text{ }^{\circ}\text{C}$ using a Fomblin oil as the adhesive and transferred to a goniometer head using cryotongs (Hampton Research) which had been cooled to $-196\text{ }^{\circ}\text{C}$ in liquid N_2 .⁵¹

Collection and Reduction of X-ray Data. Single crystals were centered on a SMART APEX II diffractometer, equipped with an APEX II 4K charge-coupled device (CCD) and a triple-axis goniometer, controlled by the APEX2 Graphical User Interface (GUI) software.⁵² Graphite-monochromated $\text{Mo K}\alpha$ radiation ($\lambda = 0.71073\text{ \AA}$) was used in the case of $\text{Hg}(\text{OTeF}_5)_2$ and $\text{Hg}(\text{OTeF}_5)_2 \cdot$

1.5XeF_2 , whereas a Bruker Triumph curved crystal monochromator with a $\text{Mo K}\alpha$ source ($\lambda = 0.71073\text{ \AA}$) was used for $\text{Hg}(\text{OTeF}_5)_2 \cdot 1.5\text{KrF}_2$. The diffraction data sets consisted of a full ϕ -rotation (1010 frames collected at 0.36° intervals) at fixed $\chi = 54.74^\circ$, followed by a series of short ω scans (250 frames) at various ϕ -settings to fill the gaps for $\text{Hg}(\text{OTeF}_5)_2$ and $\text{Hg}(\text{OTeF}_5)_2 \cdot 1.5\text{XeF}_2$. The diffraction data collections consisted of a full ϕ -rotation (3474 frames collected at 0.50° intervals) at fixed $\chi = 54.74^\circ$, followed by a series of short ω scans (1935 frames) at various ϕ -settings to fill the gaps for $\text{Hg}(\text{OTeF}_5)_2 \cdot 1.5\text{KrF}_2$. The crystal-to-detector distances were 4.9540 cm , and the data collection was carried out in a 512×512 pixel mode using 2×2 pixel binning. All diffraction data were processed by use of the APEX2 GUI software,⁵² which applied Lorentz and polarization corrections to three-dimensionally integrated diffraction spots. The program SADABS⁵³ was used for scaling the diffraction data, the application of a decay correction, and an empirical absorption correction based on redundant reflections.

Solution and Refinement of the Structures. The XPREP⁵⁴ program was used to confirm the unit cell dimensions and the crystal system and space group. The structures were solved in their respective space groups by use of direct methods, and the solutions yielded the positions of all the heavy atoms as well as some of the lighter atoms. Successive difference Fourier syntheses revealed the positions of the remaining light atoms. The final refinement was obtained by introducing anisotropic parameters for all the atoms, an extinction parameter, and the recommended weighting factor. The maximum electron densities in the final difference Fourier maps were located around the heavy atoms. The PLATON program⁵⁵ could not suggest additional or alternative symmetries.

Raman Spectroscopy. Raman spectra were recorded on a Bruker RFS 100 FT-Raman spectrometer at -150 or $-155\text{ }^{\circ}\text{C}$ using 1064-nm excitation at laser powers ranging from $300\text{--}400\text{ mW}$ and 1 cm^{-1} resolution as previously described.⁵¹ A total of 1200 scans were acquired for each spectrum. Samples were contained in $1/4$ -in. o.d. FEP vessels or in $1/4$ -in. o.d. quartz tubes.

NMR Spectroscopy. Instrumentation. The ^{19}F spectrum of $\text{Hg}(\text{OTeF}_5)_2$ was recorded at $25\text{ }^{\circ}\text{C}$ on a Bruker AVANCE DRX-500 spectrometer equipped with an 11.744-T cryomagnet. The ^{19}F NMR spectrum was acquired using a 5-mm combination $^1\text{H}/^{19}\text{F}$ probe operating at 470.568 MHz . The ^{19}F spectrum was recorded in a 32K memory, with a spectral width setting of 24 kHz , yielding a data-point resolution of $0.73\text{ Hz/data point}$ and an acquisition time of 0.68 s . The pulse width, corresponding to bulk magnetization tip angles of $\sim 90^\circ$, was $7.7\text{ }\mu\text{s}$. A relaxation delay of 2 s was used, and 1200 transients were accumulated. A line broadening of 0.3 Hz was used in the exponential multiplication of the free induction decay prior to Fourier transformation. The ^{19}F spectrum was referenced externally at room temperature ($25\text{ }^{\circ}\text{C}$) to a sample of neat CFCl_3 . The chemical shift convention used is that a positive (negative) sign indicates a chemical shift to high (low) frequency of the reference compound.

NMR Sample Preparation. A $\text{Hg}(\text{OTeF}_5)_2$ sample was prepared in a precision thin-wall Pyrex glass NMR sample tube (Wilmad) as previously described.²⁵ The NMR sample tube was fused to a $1/4$ -in. Pyrex glass tube which was connected to a grease-free 6-mm J. Young glass stopcock outfitted with a Teflon barrel using a $1/4$ -in. stainless steel Swagelok Ultratorr union fitted with Viton elastomer O-rings and was rigorously dried under dynamic vacuum. The CD_2Cl_2 solvent was distilled into the vessel at $-78\text{ }^{\circ}\text{C}$ before the sample was transferred into a drybox where $\text{Hg}(\text{OTeF}_5)_2$ was added to the frozen solvent at $-140\text{ }^{\circ}\text{C}$. The union and valve assembly were replaced, and the reactor was attached to a vacuum manifold where the NMR sample tube was cooled to $-196\text{ }^{\circ}\text{C}$, heat-sealed under dynamic vacuum, and stored at $-78\text{ }^{\circ}\text{C}$ until the ^{19}F NMR spectrum could be obtained. The sample was dissolved at $25\text{ }^{\circ}\text{C}$ just prior to data acquisition.

Computational Details. The optimized gas-phase geometry and vibrational frequencies of $\text{Hg}(\text{OTeF}_5)_2$ were calculated at the B3LYP and PBE1PBE levels of theory using two different basis sets. The aug-cc-pVTZ basis sets were used for H, O, and F, whereas aug-cc-pVTZ-(PP) basis sets having pseudopotentials were used for Hg and Te and the def2-TZVPP basis sets for H, O, F, Hg, and Te. The optimized

gas-phase geometries and vibrational frequencies of $[\text{Hg}(\text{OTeF}_5)_2]_3$ and $[\text{Hg}(\text{OTeF}_5)_2]_3 \cdot 2\text{NgF}_2$ (Ng = Xe, Kr) were only calculated using the PBE1PBE/def2-TZVPP (H, O, F, Kr, Te, Xe, and Hg) method due to the large sizes of these molecules. The noble-gas difluorides, NgF_2 (Ng = Xe, Kr), were also calculated for comparison using the PBE1PBE/def2-TZVPP method. All basis sets were obtained online from the EMSL Basis Set Exchange (<https://bse.pnl.gov/bse/portal>).^{56–61} The NBO analyses^{62–65} were performed for the PBE1PBE optimized local minima. Quantum-chemical calculations were carried out using the program Gaussian 09⁶⁶ for geometry optimizations, vibrational frequencies, and their intensities. All geometries were fully optimized using analytical gradient methods. The program GaussView⁶⁷ was used to visualize the vibrational displacements that form the basis for the vibrational mode descriptions given in Tables 4–6 and S1–S5.

■ ASSOCIATED CONTENT

Supporting Information

Complementary discussion for the preparation of high-purity HgF_2 ; Raman spectrum of pure $\text{Hg}(\text{OTeF}_5)_2$ (Figure S1); Raman spectrum of sublimed $\text{Hg}(\text{OTeF}_5)_2$ (Figure S2); crystal packing for $\text{Hg}(\text{OTeF}_5)_2$ along the *c*- and *a*-axes (Figure S3); crystal structure of $\text{Hg}(\text{OTeF}_5)_2 \cdot 1.5\text{XeF}_2$ (Figure S4); experimental Raman frequencies and intensities, calculated vibrational frequencies, and infrared and Raman intensities and detailed assignments of the Raman spectra for $\text{Hg}(\text{OTeF}_5)_2$ (exptl and calcd) (Table S1), $\text{Hg}(\text{OTeF}_5)_2$ (exptl) and $[\text{Hg}(\text{OTeF}_5)_2]_3$ (calcd) (Table S2), $\text{Hg}(\text{OTeF}_5)_2 \cdot 1.5\text{XeF}_2$ (exptl) and $[\text{Hg}(\text{OTeF}_5)_2]_3 \cdot 2\text{XeF}_2$ (calcd) (Table S3), $\text{Hg}(\text{OTeF}_5)_2 \cdot 1.5\text{KrF}_2$ (exptl) and $[\text{Hg}(\text{OTeF}_5)_2]_3 \cdot 2\text{KrF}_2$ (calcd) (Table S4); experimental and calculated Raman frequencies for XeF_2 (Table S5) and KrF_2 (Table S6); experimental ($\text{Hg}(\text{OTeF}_5)_2$) and calculated (monomer $\text{Hg}(\text{OTeF}_5)_2$) bond lengths and bond angles (Table S7); fully labeled calculated geometry of $[\text{Hg}(\text{OTeF}_5)_2]_3$ (Figure S5); fully labeled calculated geometries of $[\text{Hg}(\text{OTeF}_5)_2]_3 \cdot 2\text{NgF}_2$ (Figure S6); NBO valencies, bond orders, and NPA charges for $\text{Hg}(\text{OTeF}_5)_2$, $[\text{Hg}(\text{OTeF}_5)_2]_3$, and $[\text{Hg}(\text{OTeF}_5)_2]_3 \cdot 2\text{NgF}_2$ (Table S8); complementary discussion for the preparation of HOTeF_5 ; X-ray crystallographic files in CIF format for the structure determinations of $\text{Hg}(\text{OTeF}_5)_2$ and $\text{Hg}(\text{OTeF}_5)_2 \cdot 1.5\text{NgF}_2$ (Ng = Xe, Kr). This information is available free of charge via the Internet at <http://pubs.acs.org/>.

■ AUTHOR INFORMATION

Corresponding Author

schroblil@mcmaster.ca

Notes

The authors declare no competing financial interest.

■ ACKNOWLEDGMENTS

We thank the Natural Sciences and Engineering Research Council of Canada for support in the form of a Discovery Grant (G.J.S.), and for the award of Undergraduate Summer Research Awards (2011–13) (J.R.D.), the Ontario Graduate Scholarship in Science and Technology for support in the form of a scholarship (J.R.D.), and the computational resources provided by SHARCNet (Shared Hierarchical Academic Research Computing Network; www.sharcnet.ca). We also thank J. P. Paxon for preliminary work on some of the systems described in this work.

■ REFERENCES

- (1) Brock, D. S.; Schrobilgen, G. J.; Žemva, B. *Noble-Gas Chemistry*. In *Comprehensive Inorganic Chemistry*; Reedijk, J., Poeppelmeier, K., Eds.; Elsevier: Oxford, 2013; Vol 1, Chapter 1.25, pp 755–822.
- (2) Lehmann, J. F.; Dixon, D. A.; Schrobilgen, G. J. *Inorg. Chem.* **2001**, *40*, 3002–3017.
- (3) Elliott, H. St. A.; Lehmann, J.; Mercier, H. P. A.; Jenkins, H. D.; Schrobilgen, G. J. *Inorg. Chem.* **2010**, *49*, 8504–8523.
- (4) Brock, D. S.; Casalis de Pury, J. J.; Mercier, H. P. A.; Schrobilgen, G. J.; Silvi, B. *Inorg. Chem.* **2010**, *49*, 6673–6689.
- (5) Tavčar, G.; Tramšek, M.; Bunič, T.; Benkič, P.; Žemva, B. *J. Fluorine Chem.* **2004**, *125*, 1579–1584.
- (6) Tramšek, M.; Žemva, B. *J. Fluorine Chem.* **2006**, *127*, 1275–1284.
- (7) Tavčar, G.; Žemva, B. *Inorg. Chem.* **2005**, *44*, 1525–1529.
- (8) Bunič, T.; Tramšek, M.; Goreshnik, E.; Tavčar, G.; Žemva, B. *Inorg. Chem.* **2007**, *46*, 5276–5282.
- (9) Bunič, T.; Tramšek, M.; Goreshnik, E.; Žemva, B. *Solid State Sci.* **2008**, *10*, 1511–1516.
- (10) Tavčar, G.; Benkič, P.; Žemva, B. *Inorg. Chem.* **2004**, *43*, 1452–1457.
- (11) Bunič, T.; Tavčar, G.; Tramšek, M.; Žemva, B. *Inorg. Chem.* **2006**, *45*, 1038–1042.
- (12) Tavčar, G.; Goreshnik, E.; Mazej, Z. *J. Fluorine Chem.* **2006**, *127*, 1368–1373.
- (13) Tavčar, G.; Goreshnik, E.; Mazej, Z. *Abstracts of Papers*. Group 12 Coordination Chemistry with Fluoride Ligands. Presented at the 2011 National Meeting of the Slovenian Chemical Society; Slovenian Chemistry Days (Slovenski Kemijski Dnevi), Portorož, Slovenia, September 14–16, 2011; Paper, Anorganska Kemija in Strukturna Kemija ter Gradiva, p 69.
- (14) Tavčar, G.; Goreshnik, E. *Abstracts of Papers*. Mercury Ion as a Center for Coordination of the XeF_2 Ligand. Presented at the 17th European Symposium on Fluorine Chemistry, Paris, France, July 21–25, 2013; Poster P2.46.
- (15) Brock, D. S.; Casalis de Pury, J. J.; Mercier, H. P. A.; Schrobilgen, G. J.; Silvi, B. *J. Am. Chem. Soc.* **2010**, *132*, 3533–3542.
- (16) Holloway, J. H.; Schrobilgen, G. J.; Taylor, P. J. *Chem. Soc., Chem. Commun.* **1975**, *2*, 40–41.
- (17) Holloway, J. H.; Schrobilgen, G. J. *Inorg. Chem.* **1980**, *19*, 2632–2640.
- (18) Holloway, J. H.; Schrobilgen, G. J. *Inorg. Chem.* **1981**, *20*, 3363–3368.
- (19) Christie, K. O.; Wilson, W. W.; Bougon, R. A. *Inorg. Chem.* **1986**, *13*, 2163–2169.
- (20) Tucker, P. A.; Taylor, P. A.; Holloway, J. H.; Russell, D. R. *Acta Crystallogr.* **1975**, *B31*, 906–908.
- (21) Sladky, F.; Kropshofer, H. *Inorg. Nucl. Chem. Lett.* **1972**, *8*, 195–197.
- (22) Birchall, T.; Myers, R. D.; de Waard, H.; Schrobilgen, G. J. *Inorg. Chem.* **1982**, *21*, 1068–1073.
- (23) Riedel, S.; Kaupp, M. *Coord. Chem. Rev.* **2009**, *253*, 606–624.
- (24) Mercier, H. P. A.; Moran, M. D.; Schrobilgen, G. J.; Steinberg, C.; Suontamo, R. J. *J. Am. Chem. Soc.* **1994**, *116*, 2921–2937.
- (25) Mercier, H. P. A.; Moran, M. D.; Schrobilgen, G. J.; Steinberg, C.; Suontamo, R. J. *J. Am. Chem. Soc.* **2004**, *126*, 5533–5548.
- (26) Mercier, H. P. A.; Moran, M. D.; Sanders, J. C. P.; Schrobilgen, G. J.; Suontamo, R. J. *Inorg. Chem.* **2005**, *44*, 49–60.
- (27) Ebert, F.; Woitinek, H. Z. *Anorg. Allg. Chem.* **1933**, *210*, 269–272.
- (28) Seppelt, K.; Nothe, D. *Inorg. Chem.* **1973**, *11*, 2727–2730.
- (29) Sladky, F.; Kropshofer, H.; Leitzke, O.; Peringer, P. J. *Inorg. Nucl. Chem., H. H. Hyman Memorial Volume* **1976**, 69–71.
- (30) Riedel, S.; Straka, M.; Kaupp, M. *Chem.—Eur. J.* **2005**, *11*, 2743–2755.
- (31) Bondi, A. J. *Phys. Chem.* **1964**, *68*, 441–451.
- (32) Fir, B. A.; Mercier, H. P. A.; Sanders, J. C. P.; Dixon, D. A.; Schrobilgen, G. J. *J. Fluorine Chem.* **2001**, *110*, 89–107.

- (33) Cordero, B.; Gómez, V.; Platero-Prats, A. E.; Revés, M.; Echeverría, J.; Cremades, E.; Barragán, F.; Alvarez, S. *Dalton Trans.* **2008**, 2832–2838.
- (34) Hughes, M. J.; Mercier, H. P. A.; Schrobilgen, G. J. *Inorg. Chem.* **2009**, *48*, 4478–4490.
- (35) Nieboer, J.; Mack, J. P.; Mercier, H. P. A.; Gerken, M. *Inorg. Chem.* **2010**, *49*, 6153–6159.
- (36) Hughes, M. J.; Brock, D. S.; Mercier, H. P. A.; Schrobilgen, G. J. *J. Fluorine Chem.* **2011**, *132*, 660–668.
- (37) Agron, P. A.; Begun, G. M.; Levy, H. A.; Mason, A. A.; Jones, C. G.; Smith, D. F. *Science* **1963**, *139*, 842–844.
- (38) Al-Mukhtar, M.; Holloway, J. H.; Hope, E. G.; Schrobilgen, G. J. *J. Chem. Soc., Dalton Trans.* **1991**, 2831–2834.
- (39) Turner, J. J.; Pimentel, G. C. *Science* **1963**, *140*, 974–975.
- (40) Benkič, P.; Tramšek, M.; Žemva, B. *Solid State Sci.* **2002**, *4*, 1425–1434.
- (41) Tramšek, M.; Benkič, P.; Žemva, B. *Angew. Chem., Int. Ed.* **2004**, *43*, 3456–3458.
- (42) Bertolini, J. C. *J. Emerg. Med.* **1992**, *10*, 163–168.
- (43) Peters, D.; Mietchen, R. *J. Fluorine Chem.* **1996**, *79*, 161–165.
- (44) Segal, E. B. *Chem. Health Saf.* **2000**, 18–23.
- (45) Casteel, W. J., Jr.; Dixon, D. A.; Mercier, H. P. A.; Schrobilgen, G. J. *Inorg. Chem.* **1996**, *35*, 4310–4322.
- (46) Mercier, H. P. A.; Sanders, J. C. P.; Schrobilgen, G. J.; Tsai, S. S. *Inorg. Chem.* **1993**, *32*, 386–393.
- (47) Kinkead, S. A.; FitzPatrick, J. R.; Foropoulos, J., Jr.; Kissane, R. J.; Purson, J. D. In *Fluorine Chemistry Toward the 21st Century*; Thrasher, J. S., Strauss, S. H., Eds.; ACS Symposium Series 555; American Chemical Society: Washington, DC, 1994; Chapter 3, pp 40–55.
- (48) Lehmann, J. F.; Mercier, H. P. A.; Schrobilgen, G. J. *Coord. Chem. Rev.* **2002**, 233–234, 1–39.
- (49) Emar, A. A. A.; Schrobilgen, G. J. *Inorg. Chem.* **1992**, *31*, 1323–1332.
- (50) Schack, C.; Wilson, R. D. *Inorg. Chem.* **1970**, *9*, 311–314.
- (51) Gerken, M.; Dixon, D. A.; Schrobilgen, G. J. *Inorg. Chem.* **2000**, *39*, 4244–4255.
- (52) APEX2, release v2011.6-1; Bruker AXS Inc.: Madison, WI, 1995.
- (53) Sheldrick, G. M. SADABS (*Siemens Area Detector Absorption Corrections*), version 2.03; Siemens Analytical X-ray Instruments, Inc.: Madison, WI, 1999.
- (54) Sheldrick, G. M. *SHELXTL-Plus, release 5.1*; Siemens Analytical X-ray Instruments, Inc.: Madison, WI, 1998.
- (55) Spek, A. L. *J. Appl. Crystallogr.* **2003**, *36*, 7–13.
- (56) Basis sets and pseudopotentials were obtained from the Extensible Computational Chemistry Environment Basis set Database, version 2/25/04, as developed and distributed by the Molecular Science Computing Facility, Environmental and Molecular Science Laboratory, which is part of the Pacific Northwest Laboratory, P.O. Box 999, Richland, WA 99352.
- (57) Dunning, T. H., Jr. *J. Chem. Phys.* **1989**, *90*, 1007–1023.
- (58) Kendall, R. A.; Dunning, T. H., Jr.; Harrison, R. J. *J. Chem. Phys.* **1992**, *96*, 6796–6806.
- (59) Peterson, K. A.; Figgen, D.; Goll, E.; Stoll, H.; Dolg, M. *J. Chem. Phys.* **2003**, *119*, 11113–11123.
- (60) Peterson, K. A.; Puzzarini, C. *Theor. Chem. Acc.* **2005**, *114*, 283–296.
- (61) Weigend, F.; Ahlrichs, R. *Phys. Chem. Chem. Phys.* **2005**, *7*, 3297–3305.
- (62) Reed, A. E.; Weinstock, R. B.; Weinhold, F. *J. Chem. Phys.* **1985**, *83*, 735–746.
- (63) Reed, A. E.; Curtiss, L. A.; Weinhold, F. *Chem. Rev.* **1998**, *88*, 899–926.
- (64) Glendening, E. D.; Reed, A. E.; Carpenter, J. E.; Weinhold, F. *NBO Version 3.1*; Gaussian Inc.: Pittsburgh, PA, 1990.
- (65) Glendening, E. D.; Badenhoop, J. K.; Reed, A. E.; Carpenter, J. E.; Bohmann, C. M.; Morales, C. M.; Weinhold, F. *NBO Version 5.0*; Theoretical Chemistry Institute, University of Wisconsin: Madison, WI, 2001.
- (66) Frisch, M. J.; Trucks, G. W.; Schlegel, H. B.; Scuseria, G. E.; Robb, M. A.; Cheeseman, J. R.; Scalmani, G.; Barone, V.; Mennucci, B.; Petersson, G. A.; Nakatsuji, H.; Caricato, M.; Li, X.; Hratchian, H. P.; Izmaylov, A. F.; Bloino, J.; Zheng, G.; Sonnenberg, J. L.; Hada, M.; Ehara, M.; Toyota, K.; Fukuda, R.; Hasegawa, J.; Ishida, M.; Nakajima, T.; Honda, Y.; Kitao, O.; Nakai, H.; Vreven, T.; Montgomery, J. A., Jr.; Peralta, J. E.; Ogliaro, F.; Bearpark, M.; Heyd, J. J.; Brothers, E.; Kudin, K. N.; Staroverov, V. N.; Kobayashi, R.; Normand, J.; Raghavachari, K.; Rendell, A.; Burant, J. C.; Iyengar, S. S.; Tomasi, J.; Cossi, M.; Rega, N.; Millam, N. J.; Klene, M.; Knox, J. E.; Cross, J. B.; Bakken, V.; Adamo, C.; Jaramillo, J.; Gomperts, R.; Stratmann, R. E.; Yazyev, O.; Austin, A. J.; Cammi, R.; Pomelli, C.; Ochterski, J. W.; Martin, R. L.; Morokuma, K.; Zakrzewski, V. G.; Voth, G. A.; Salvador, P.; Dannenberg, J. J.; Dapprich, S.; Daniels, A. D.; Farkas, Ö.; Foresman, J. B.; Ortiz, J. V.; Cioslowski, J.; Fox, D. J. *Gaussian 09*, revision D.01; Gaussian, Inc.: Wallingford, CT, 2009.
- (67) *GaussView*, release 3.0; Gaussian Inc.: Wallingford, CT, 2003.